Case Studies in Thermal Engineering 73 (2025) 106485

Contents lists available at ScienceDirect

Case Studies in Thermal Engineering

journal homepage: www.elsevier.com/locate/csite

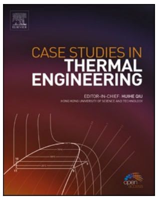

# Comparison of $O_2$-enriched and $N_2O$ oxidizers on dual-flame structure and entropy generation

Yueh-Heng Li [a,b,*], Po-Hung Lin [a], Wen-Yuan Tsai [a], Janusz Lasek [c]

[a] *Department of Aeronautics and Astronautics, National Cheng Kung University, Tainan, 701, Taiwan*
[b] *International Master Degree Program on Energy Engineering, National Cheng Kung University, Tainan, 701, Taiwan*
[c] *Institute of Energy and Fuel Processing Technology, ul. Zamkowa 1, 41-803 Zabrze, Poland*

## ARTICLE INFO

Handling Editor: Dr Y Su

*Keywords:*
Triple-port burner
Dual-flame structure
Oxygen-enriched combustion
Entropy generation rate
Nitrous oxide

## ABSTRACT

This study utilizes a triple concentric burner to generate a dual-flame structure and investigates the impact of dual flames on entropy generation under varying fuel-oxidizer velocity ratio (R), ultimately identifying the dominant pathways. The study also examined the substitution of nitrous oxide ($N_2O$) with a nitrogen-oxygen ($N_2{-}O_2$) mixture to understand the influence of $N_2O$ decomposition on entropy generation. The research evaluated the irreversibility of chemical reactions in the presence of a dual-flame structure. It was observed that the chemical reaction term in the $N_2O$ case ($R = 3$) was approximately twice as intense as in the $O_2$-enriched case ($R = 5$) due to the more vigorous reaction of $N_2O$, despite similar energy input. Reactions involving $N_2O$, such as those related to the cyanato radical (NCO) and isocyanic acid (HNCO), were slightly more pronounced in the $N_2O$ case compared to the $O_2$-enriched case, even though the R ratio was lower in the $N_2O$ case. In conclusion, increased entropy generation reduces exergy and decreases second-law efficiency (ηII) from 88.5 % to 78.8 % in $O_2$-enriched cases and from 74.3 % to 66.3 % in $N_2O$ cases as R increases. This decrease is more pronounced in dual-flame structures, where $\eta_{II}$ drops below 80 %, primarily due to heat conduction and chemical reactions.

## Nomenclature

| | |
|---|---|
| $A$ | Pre-exponential factor, 1/s |
| $\dot{A}_{in}$ | Incoming exergy, W |
| $\dot{A}_{out}$ | Remaining exergy, W |
| $a_i$ | Specific availability of species *i*, J/kg |
| $a_i^{ch}$ | Specific chemical availability of species *i*, J/kg |
| $B$ | Temperature exponent |
| $D_m$ | Effective binary diffusivity of species *i* in the mixture *m*, $m^2/s$ |
| $D_{i,m}$ | Binary diffusivity of species *i* and *m*, $m^2/s$ |
| $E_a$ | Activation energy, kJ/mol |
| $R$ | Fuel-oxidizer velocity ratio |
| $f_i$ | Body force of species *i*, $kg/m^2s^2$ |
| $g$ | Gravity, $m/s^2$ |
| $h_i$ | Specific enthalpy of species *i*, J/kg |

(*continued on next page*)

---

[*] Corresponding author. Department of Aeronautics and Astronautics, National Cheng Kung Univ., Tainan, 701, Taiwan.
*E-mail addresses:* yueheng@mail.ncku.edu.tw, yuehheng.li@gmail.com (Y.-H. Li).

https://doi.org/10.1016/j.csite.2025.106485
Received 6 March 2025; Received in revised form 8 May 2025; Accepted 8 June 2025

(*continued*)

| | |
|---|---|
| $\dot{\boldsymbol{I}}$ | Irreversibility, W |
| $J_i$ | Mass flux of species *i,* kg/m$^2$s |
| $k$ | Reaction constant, m$^3$/kgs |
| $k_b$ | Boltzmann constant, m$^2$kg/s$^2$K |
| $M_i$ | Molecular weight of species *i* |
| $M_m$ | Molecular weight of species *m* |
| $\dot{\boldsymbol{m}}$ | Mass flow rate, kg/s |
| $P$ | Pressure, Pa |
| $\boldsymbol{qc}$ | Conduction heat flux, W/m$^2$ |
| $R_g$ | Gas constant, J/kg · K |
| $R_u$ | Universal gas constant, J/kmol · K |
| $r$ | Radial coordinate, m |
| $s_i$ | Specific entropy of species *i,* J/kg · K |
| $T$ | Temperature, K |
| $T^*$ | Reduced temperature, K |
| $\boldsymbol{u}$ | Velocity vector, m/s |
| $v$ | Velocity, m/s |
| $X_i$ | Mole fraction of species *i* |
| $Y_i$ | Mass fraction of species *i* |
| $Z$ | Axial distance above the burner tip, m |
| $z$ | Axial coordinate, m |
| **Greek symbols** | |
| $\eta_{II}$ | Second-law efficiency |
| $\Lambda$ | Thermal conductivity, W/mK |
| $\mu_i$ | Chemical potential of species *I,* J/kg |
| $\rho$ | Density, kg/m$^3$ |
| $\boldsymbol{\sigma}'$ | Integral entropy generation rate, W/K |
| $\boldsymbol{\sigma}''$ | Volumetric entropy generation rate, W/m$^3$K |
| $\sigma_{i,m}$ | Collision diameter of species *i* and *m,* m |
| $\boldsymbol{\tau}$ | Viscous stress, N/m$^2$ |
| $\Delta\upsilon$ | Reaction rate, kg/m$^3$ s |
| $\Omega$ | Collision integral |
| $\dot{\boldsymbol{\omega}}_{\boldsymbol{i}}$ | Production rate of species *i,* kg/m$^3$s |
| **Subscripts** | |
| *C* | Coflow |
| *chem* | Chemical reaction |
| *cond* | Heat conduction |
| *diff* | Mass diffusion |
| *F* | Fuel |
| *max* | Maximum |
| *mix* | Mixture |
| *ref* | Reference |
| *tot* | Total |
| *O* | Oxidizer |
| *vis* | Viscous dissipation |
| **Chemical Species and Compounds** | |
| $N_2O$ | Nitrous oxide |
| $O_2$ | Oxygen |
| $N_2$ | Nitrogen |
| $CH_4$ | Methane |
| $CO_2$ | Carbon dioxide |
| $H_2O$ | Water |
| $HNCO$ | Isocyanic acid |
| $NCO$ | Cyanato radical |
| $HO_2$ | Hydroperoxyl radical |
| $H_2$ | Hydrogen |
| $OH$ | Hydroxyl radical |
| $CH_3$ | Methyl radical |
| $CH_2O$ | Formaldehyde |
| $HCO$ | Formyl radical |
| $CO$ | Carbon monoxide |
| $CH_2CO$ | Ketene |
| $NH$ | Imidogen radical |
| $NH_2$ | Amino radical |
| $N_2H_4$ | Hydrazine |
| $H_2O_2$ | Hydrogen peroxide |
| $ADN$ | Ammonium dinitramide |
| $HAN$ | Hydroxylammonium nitrate |

## 1. Introduction

Environmental concerns have led to the global pursuit of cleaner energy solutions, including hydrogen[1,2], ammonia [1,3–5], biofuels [6–9] and iron particles [10,11], across various sectors such as aerospace propulsion. In this context, replacing toxic propellants like hydrazine ($N_2H_4$) has gained significant attention. Researchers are exploring several substitutes, including hydrogen peroxide ($H_2O_2$) [12], ammonium dinitramide (ADN)-based fuels (e.g., LMP-103S), hydroxylammonium nitrate (HAN)-based propellants (e.g., AF-M315E/ASCENT) [13], water electrolysis propulsion methods, and fuel blends incorporating nitrous oxide ($N_2O$) [14,15,16]. Among these, $N_2O$-based fuel mixtures have received relatively less attention, prompting increased research focus. $N_2O$ is particularly promising as an oxidizer due to its oxygen-enriching properties and the significant exothermicity of its self-decomposition reaction [17,18], expressed as:

$$N_2O \rightarrow N_2 + 0.5\,O_2 + 81.97\ (\mathrm{kJ\,/\,kmol}) \qquad \text{Eq. 1}$$

However, its role in influencing entropy generation—a key parameter in evaluating second-law efficiency—remains insufficiently explored. Numerous studies have advanced the understanding of $N_2O$-based combustion. Vandooren et al. [19] compared methane ($CH_4$)–oxygen ($O_2$) and $CH_4$–$N_2O$ flames, identifying key species influencing flame formation. Newman-Lehman et al. [20] examined the structure and extinction of $CH_4$–$N_2O$ and ethane ($C_2H_6$)–$N_2O$ flames, noting that higher $N_2O$ fractions reduced burning velocity. Powell et al. [21] emphasized the importance of adjusting the reaction rate constant for $N_2O$ and hydrogen radical (H) to accurately simulate laminar flame speed in $N_2O$-hydrocarbon flames. Razus et al. [22] compiled a comprehensive database to support the development and validation of chemical kinetic models for fuel–$N_2O$ reaction systems. Similarly, Wang and Zhang [23] refined a reaction mechanism for ethylene ($C_2H_4$)–$N_2O$ flames through sensitivity analysis, enabling accurate prediction of laminar burning velocity. Shebeko et al. [24] demonstrated that $N_2O$, as an oxidizer, significantly extends the flammability limits of hydrogen ($H_2$)–$N_2O$ and $CH_4$–$N_2O$ flames. Beyond flame characteristics, Li et al. [25–27] found that $N_2O$ decomposition influences soot temperature and the balance between soot formation and oxidation. Notably, Li et al. [1] validated a measurement technique through numerical simulations, proposing its use for verifying chemical mechanisms in premixed $N_2O$ flames.

Energy efficiency is a critical performance metric in combustion systems, driving research to maximize conversion efficiency for a given energy input. Entropy analysis provides a robust method for evaluating energy efficiency by quantifying the entropy generation rate ($\sigma$), which measures energy dissipation due to irreversible processes. Higher σ values lead to increased exergy loss and reduced second-law efficiency ($\eta_{II}$). Several studies have explored σ in combustion processes. Cai et al. [28] point out that incorporating a bluff-body in hydrogen-fueled meso-scale combustors significantly enhances flame stability and fuel mixing efficiency, thereby optimizing thermal performance and improving exergy efficiency, reducing exergy losses, and providing an effective approach for high-efficiency energy conversion. Guan et al. [29] point out that entropy generation in a bifurcating thermoacoustic combustor is predominantly driven by temperature fluctuations near the flame, contributing significantly to the system's irreversibility and highlighting the need for effective entropy management to enhance combustor efficiency. Arpaci and Selamet [30] derived an entropy generation equation for one-dimensional flames, advocating the use of established flame structure models for real flame entropy analysis. Nishida et al. [31] analyzed σ in a one-dimensional laminar diffusion flame during head-on quenching, identifying chemical reactions as the primary contributor to σ, with heat conduction becoming dominant near quenching. Safari et al. [32,33] investigated the effect of $H_2$ addition on σ in non-premixed $CH_4$–air flames, finding that higher $H_2$ fractions reduce σ due to simpler reaction pathways involving fewer minor species, although heat conduction increases with rising temperatures. In the section on burner selection, the triple port burner is favored for its superior attributes, including enhanced mixing efficiency, greater flame stability, lower emissions, and adaptability across various industrial applications. As a result, many researchers [34,35] have employed triple port burners in combustion studies to leverage these benefits. Chou et al. [36] conducted numerical simulations using a triple-port burner to study σ in $CH_4$–$N_2O$ diffusion flames, revealing that $N_2O$ decomposition significantly enhances irreversibility, primarily through intensified chemical reactions driven by thermal effects. Yu and Wu [37] developed a novel approach to quantify non-equilibrium σ in premixed stretched $CH_4$ flames, showing that strain rate strongly influences chemical irreversibility, while pressure and temperature affect heat conduction, mass diffusion, and chemical irreversibility. They also proposed an empirical formula for predicting irreversibility based on flame thickness, applicable to various fuel mixtures. Datta [38] explored the relationship between σ and gravitational levels, noting that heat conduction increases with gravity, while low-gravity conditions yield a more uniform temperature distribution, reducing σ. Zhang et al. [39] analyzed σ and exergy loss in an ethylene co-flow diffusion flame, demonstrating that soot significantly impacts σ through thermal radiation. Yang et al. [40] examined how inert blocks affect temperature profiles and σ in a micro combustor, providing insights into combustion dynamics. Liu et al. [41] compared σ and exergy loss in laminar premixed flames under standard and engine-like conditions, finding that chemical reactions dominate σ in autoignition flames, influenced by flame thickness and fuel consumption pathways.

Given potential of $N_2O$ as an oxidizer, calculating σ is crucial for optimizing its use in combustion systems. This study employs numerical simulations to investigate σ in $CH_4$–$N_2O$ diffusion flames, analyzing contributions from viscous dissipation, heat conduction, mass diffusion, and chemical reactions. Each physical interpretation and spatial distribution of mechanism are examined. The study also explores the effect of replacing $N_2O$ with a nitrogen-oxygen ($N_2-O_2$) mixture (67 % $N_2$ + 33 % $O_2$), which maintains the same nitrogen-to-oxygen ratio (N/O = 2) as $N_2O$, to isolate the impact of $N_2O$ decomposition on σ. Additionally, the influence of increasing the central oxidizer inlet velocity is assessed, as it can alter flame structure, potentially forming a dual-flame configuration with an inner inverse diffusion or partially premixed flame and an outer normal diffusion flame. By quantifying irreversibility, this study provides insights into optimizing combustion efficiency and minimizing energy loss in $N_2O$-based propulsion systems.

## 2. Numerical simulation setup

### 2.1. Numerical model

To analyze the entropy generation rate ($\sigma$) of a methane ($CH_4$)–nitrous oxide ($N_2O$) diffusion flame, this study employs the commercial computational fluid dynamics software Star-CCM+. To enhance computational efficiency, the flame is modeled within a two-dimensional framework. The simulation is governed by fundamental equations, including the two-dimensional Navier–Stokes equations, steady-state formulations, species transport equations for individual chemical constituents, and conservation laws for mass and energy.

Diffusion in multicomponent mixtures is modeled using a generalized approximation that extends Fick's law for binary diffusion to account for all species except one, reformulating the species diffusion flux or velocity equation. The dynamic viscosity, specific heat, and thermal conductivity of the multicomponent gas are calculated using the mass-weighted averaging method. A key parameter in this framework is the effective binary diffusivity of species $i$ in the mixture m, derived from kinetic theory as follows:

$$D_m = \frac{1\text{-}X_i}{\sum\limits_{i=1, i\neq m} \frac{X_i}{D_{i,m}}} \tag{Eq. 2}$$

Here, $D_m$ represents the effective binary diffusivity ($m^2/s$), $X_i$ denotes the mole fraction of species $i$, and $D_{i,m}$ signifies the binary diffusivity of species $i$ and m ($m^2/s$). The binary diffusivity $D_{i,m}$ is computed using the Chapman–Enskog equation [42], which describes molecular interactions in gases, as follows:

$$D_{i,m} = \frac{2.66 \times 10^{-7} T^{3/2}}{P M_{i,m}^{1/2} \sigma_{i,m}^2 \Omega(T^*)} \tag{Eq. 3}$$

where the reduced molecular weight $M_{i,m}$ is defined as:

$$M_{i,m} = \frac{2 M_i M_m}{M_i + M_m} \tag{Eq. 4}$$

In these equations, $M_i$ and $M_m$ are the molecular weights of species $i$ and $m$ (kg/kmol), respectively; $T$ is the temperature (K); $P$ is the static pressure (Pa); $\sigma_{i,m}$ is the collision diameter (m) for the species pair $i$ and $m$, representing the effective distance between colliding molecules; and $\Omega(T^*)$ is the collision integral, a dimensionless function of the reduced temperature $T^*$. The reduced temperature is defined as:

$$T^* = \frac{kT}{\varepsilon_{i,m}} \tag{Eq. 5}$$

where k is the Boltzmann constant ($1.38 \times 10^{-23}$ $m^2$ $kg/s^2 \cdot K$), and $\varepsilon_{i,m}$ is the Lennard–Jones potential energy ($J$) specific to the interacting species pair $i$ and $m$, characterizing their intermolecular forces.

The simulation utilizes a coaxial triple-port burner, as illustrated in Fig. 1, to generate the diffusion flame. The burner consists of

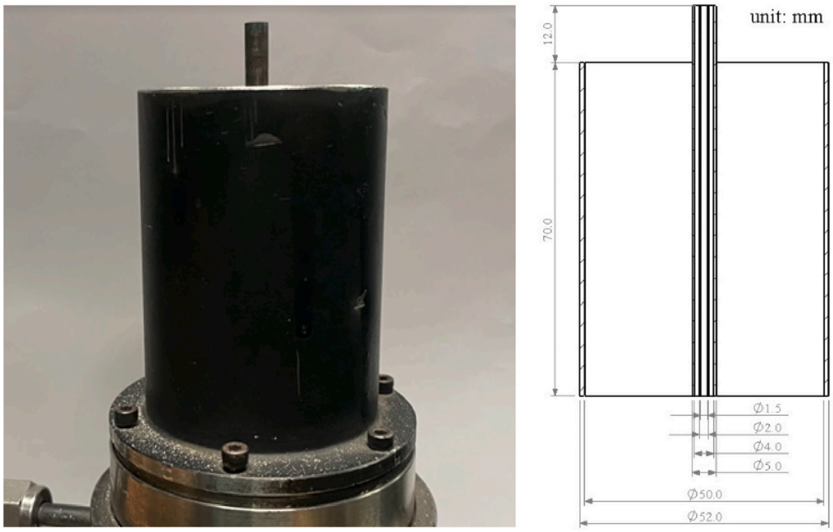

**Fig. 1.** Schematic of the adopted triple-port burner.

three concentric ports: an outer annular port supplying coflow air to stabilize and shield the flame, an inner annular port delivering $CH_4$, and a central circular port providing the oxidizer, either $N_2O$ or a nitrogen-oxygen (67 %$N_2$– 33 % $O_2$) mixture. The burner's nozzles have inner (outer) diameters of 50 (52) mm for the coflow port, 4 (5) mm for the fuel port, and 1.5 (2) mm for the oxidizer port, arranged from outermost to innermost. To promote flame stability, the fuel and oxidizer ports are designed to protrude 12 mm beyond the coflow port outlet, ensuring stable and well-defined flame development.

The fuel velocity ($v_F$) and co-flow velocity are maintained at 0.1 m/s, aligning the fuel and oxidizer ports at the same vertical level. The oxidizer velocity ($v_O$) is adjusted based on the fuel-oxidizer velocity ratio (R), defined as the ratio of oxidizer to fuel velocity. The flame length, observed to be less than 2 cm, justifies a 6 cm computational domain height for the open environment. Initial conditions include a uniform temperature of 293 K and velocity field at the inlet for the fuel, oxidizer, and co-flow. The flow remains laminar, with Reynolds numbers ranging from 17.9 to 302.9, and the outlet pressure is fixed at 101,325 Pa. Heat transfer between the combustible fluid and the stainless-steel burner wall is modeled using a coupled boundary condition.

The numerical simulation employs a nonuniform grid, with refined resolution along the centerline reaction zone to enhance accuracy. A grid independence study confirms that doubling the computational nodes results in less than 1 % variation in peak temperature and species distribution. Convergence is achieved when residuals of the governing equations fall below $10^{-5}$.

The Unified San Diego Mechanism (USM) [43] is adopted for the chemical kinetics, comprising 582 reactions and 96 species. The USM integrates the USC Mech II-2 carbon hydroxide model [44] (529 reactions) with the San Diego $N_2O$ mechanism [45] (53 reactions), with adjusted rate constants to ensure compatibility. Validated extensively [43], the USM accurately predicts combustion behavior. Li et al. [1] compared the USM and Unified GRI-Mech (UGM) mechanisms in $CH_4$–$N_2O$ premixed flames using a slot burner, finding that the USM provides more accurate predictions of laminar burning velocity. Furthermore, previous work by Li et al. [36] has experimentally validated the entropy and exergy models, establishing a solid foundation for the present study.

### 2.2. Exergy analysis

Four governing equations were used to obtain various flame characteristics, such as temperature, flame structure, velocity field, species distribution, and heat release rate. The mechanism used in the numerical simulation enabled exergy analysis to be performed through postprocessing.

An essential parameter in exergy analysis is the second-law efficiency ($\eta_{II}$), which quantifies the proportion of energy available for effective use in the combustion system. This efficiency can be mathematically expressed as follows:

$$\eta_{II} = \frac{\dot{A}_{out}}{\dot{A}_{in}} \qquad \text{Eq. 6}$$

where $\dot{\boldsymbol{A}}_{\boldsymbol{in}}$ signifies the exergy input (W) delivered by the inlet gas to the combustion system, and $\dot{\boldsymbol{A}}_{\boldsymbol{out}}$ is the remaining exergy (W) after the incoming exergy has been consumed through an irreversible process. The remained exergy can be defined as follows:

$$\dot{A}_{out} = \dot{A}_{in} - \dot{I} \qquad \text{Eq. 7}$$

where $\dot{\boldsymbol{I}}$ is the irreversibility (W) representing the irreversible processes in the combustion process. The irreversibility of the combustion process can be determined from the entropy generation rate resulting from the transport of heat, mass, and momentum and the chemical reactions in the combustion process. The general entropy transport equation can be used to calculate the entropy generation rate as follows:

$$\sigma''_{tot} = \frac{\tau : \nabla u}{T} + \frac{(\lambda \nabla T \cdot \nabla T)}{T^2} + Rg\sum_i \left(\frac{\rho D_{\mathrm{eff}}}{X_i}\right) \nabla Y_i \cdot \nabla X_i - \sum_i \frac{\mu_i \cdot \dot{\omega}_i}{T} \qquad \text{Eq. 8}$$

The equation of the entropy generation rate can be divided into five items: fluid viscosity, heat conduction, mass diffusion, body force, and the chemical reaction. Fourier's and Fick's laws were applied, and gravity was the only body force in the numerical simulation. Eq. (8) can be simplified and divided into the following expressions:

$$\sigma''_{vis} = \frac{(\tau : \nabla u)}{T} \qquad \text{Eq. 9}$$

$$\sigma''_{cond} = \frac{(\lambda \nabla T \cdot \nabla T)}{T^2} \qquad \text{Eq. 10}$$

$$\sigma'_{\mathrm{diff}} = Rg\sum_i \left(\frac{\rho D_{\mathrm{eff}}}{X_i}\right) \nabla Y_i \cdot \nabla X_i \qquad \text{Eq. 11}$$

$$\sigma''_{chem} = -\sum_i \frac{(\mu_i\, \dot{\omega}_i)}{T} \qquad \text{Eq. 12}$$

$$\sigma''_{tot} = \sigma''_{vis} + \sigma''_{cond} + \sigma''_{diff} + \sigma''_{chem} \qquad \text{Eq. 13}$$

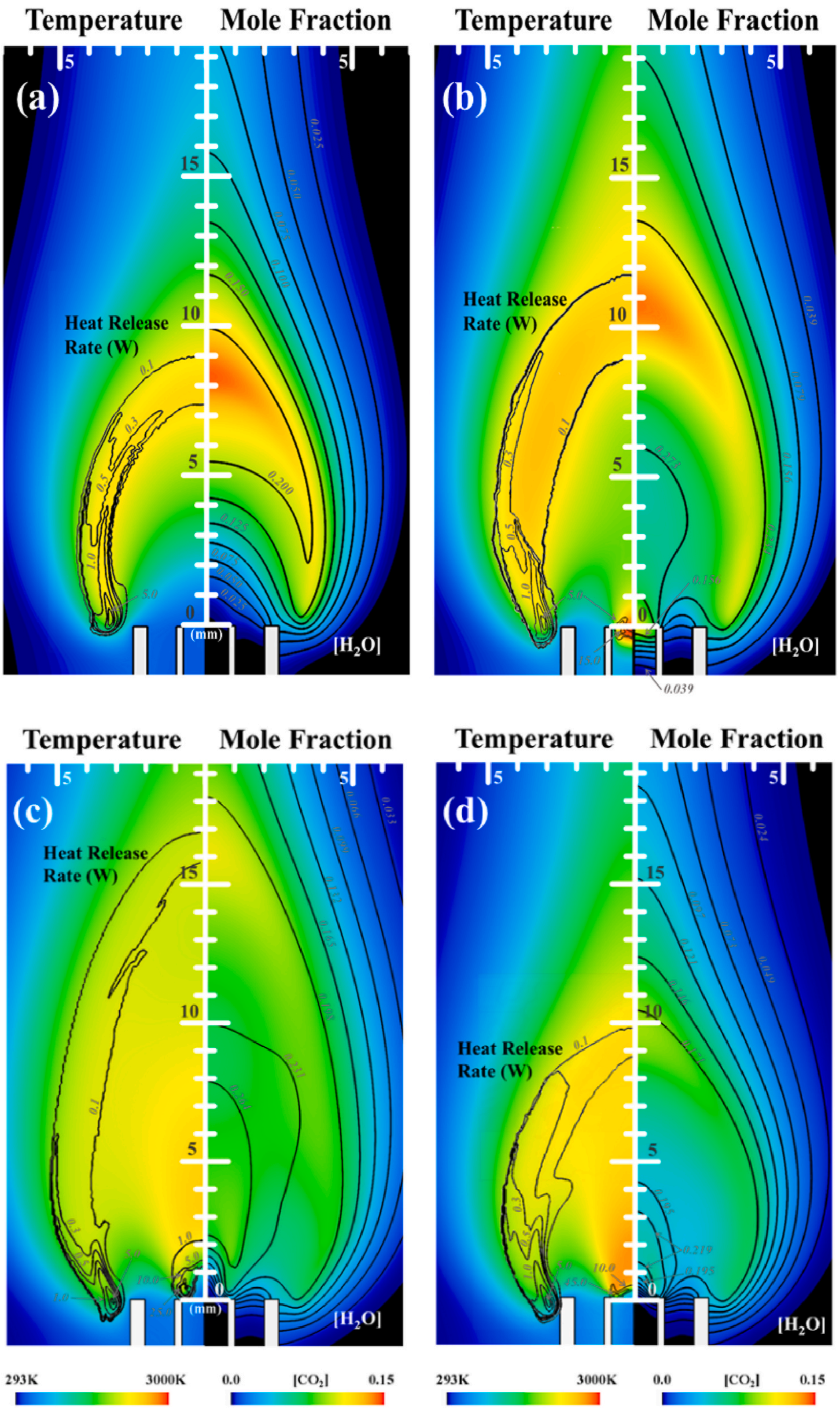

**Fig. 2.** Distributions of temperature, mole fraction of $CO_2$, rate of heat release, and mole fraction $H_2O$ are presented for the following cases: (a) oxygen-enriched mixture (67 % nitrogen ($N_2$) + 33 % oxygen ($O_2$)) at fuel-oxidizer velocity ratio (R) of 1, (b) nitrous oxide ($N_2O$) at R = 1, (c) oxygen-enriched mixture at R = 5, and (d) $N_2O$ at R = 3.

The volumetric entropy generation rate ($\sigma''$) is a key quantity, measured in W/m$^3$·K, while the viscous stress ($\tau$) and thermal conductivity ($\lambda$) are expressed in N/m$^2$ and W/m·K, respectively. The species production rate ($\dot{\omega}_i$) and effective mass diffusivity ($D_{eff}$) are also considered, quantified in W/m·K and m$^2$/s. In this framework, the velocity vector ($u$), temperature ($T$), specific gas constant ($R_g$), and density ($\rho$) are fundamental parameters representing flow dynamics and thermodynamic properties.

Furthermore, the mass fraction ($Y_i$) and mole fraction ($X_i$) characterize the distribution of species $i$, with its chemical potential ($\mu_i$) derived from Gibbs' function and mathematically defined as:

$$\mu_i = h_i(T) - Ts_i(T) + RT\, ln\left( X_i\, P \,/\, P_{ref} \right) \qquad \text{Eq. 14}$$

In this context, the total pressure is denoted by $P$ (Pa), while the reference pressure, $P_{ref}$, is set at a constant value of 101325 Pa. The specific enthalpy ($h_i$) and specific entropy ($s_i$) of species $i$ are expressed in units of J/kg and J/kg·K, respectively.

As outlined in Equation (13), the local volumetric entropy generation rate arises from four primary mechanisms: heat conduction, chemical reactions, mass diffusion, and viscous dissipation, each contributing to the overall entropy production in the system. Under the specified conditions, the impact of the viscous dissipation term is minimal and can be disregarded in the calculations. The total entropy generation rate, denoted as $\sigma'$, is determined using the following equation:

$$\sigma'_{tot} = \iint 2\pi r \sigma''_{tot} drdz \qquad \text{Eq. 15}$$

After calculating the entropy generation rate, the irreversibility should be determined for exergy analysis. The Gouy–Stodola theorem [46] provides the basis for calculating irreversibility, which can be determined using the following equation:

$$\dot{I} = T_{ref}\, \sigma'_{tot} \qquad \text{Eq. 16}$$

For this study, the reference temperature $T_{ref}$ was defined as 298 K. After determining the irreversibility from the entropy generation rate, the second-law efficiency of the combustion process can be calculated. Equation (6), which represents second-law efficiency, can be restated as follows [38]:

$$\eta_{II} = 1 - \frac{\dot{I}}{\dot{A}_{in}} \qquad \text{Eq. 17}$$

In most cases, the incoming exergy is primarily contributed by the fuel, as it serves as the energetic gas. However, in this study, $N_2O$, an energetic oxidizer, was used and demonstrated a higher chemical availability compared to the fuel. Therefore, the oxidizer also contributes to the incoming exergy when $N_2O$ is used as the oxidizer. The incoming exergy is calculated as follows:

$$\dot{A}_{in} = \frac{\dot{m}}{M_{mix}} \sum_i X_i a_i \qquad \text{Eq. 18}$$

In this context, $a_i$ represents the specific availability of species $i$ (J/kg), $M_{mix}$ denotes the molecular weight of the mixture, and $\dot{m}$ corresponds to the mass flow rate (kg/s). The specific availability $a_i$ is mathematically defined as:

$$a_i = h_i - h_{i,0} - T_0\left(s_i - s_{i,0}\right) + \frac{v^2}{2} + gz + a_i^{ch} \qquad \text{Eq. 19}$$

In this equation, $z$ corresponds to the axial distance measured from a reference height (m), $v$ represents velocity (m/s), and $g$ denotes gravitational acceleration (m/s$^2$).

Moreover, $h_{i,0}$ and $s_{i,0}$ indicate the specific enthalpy and specific entropy of species i at a reference temperature of 298 K. This study also considers the specific chemical availability of species i, denoted as $a_i^{ch}$ (J/kg) [47].

On the basis of the study of Szargut, the specific chemical availabilities of $CH_4$ and $N_2O$, which were used as incoming gases, were found to be 802.3 and 82.05 kJ/mol, respectively. $N_2$ and $O_2$, which are nonenergetic gases, have a specific chemical availability of 0. The same applies to air, which is a mixture of $N_2$ and $O_2$. However, the incoming exergy of air or $O_2$-enriched gas (67 % $N_2$ + 33 % $O_2$) is nonzero because the gas is preheated through the stainless-steel wall of the burner. Moreover, kinetic and potential energy terms were not considered because they could not be used during the combustion process. Therefore, the availability equation of each incoming species (Eq. (19)) can be simplified as follows:

$$a_i = h_i - h_{i,0} - T_0\left(s_i - s_{i,0}\right) + a_i^{ch} \qquad \text{Eqs. 20}$$

## 3. Results and discussion

### 3.1. *Structure and species distributions*

Fig. 2 presents the numerical simulation results for the diffusion flames of $CH_4$ and $N_2O$ compared to those of oxygen-enriched conditions (67 %$N_2$ + 33 % $O_2$), focusing on distributions of the mole fraction of carbon dioxide ($CO_2$), contours of the mole fraction of water ($H_2O$), rates of heat release, and profiles of temperature across three oxidizer conditions. The results compare the cases of

$O_2$-enriched conditions at ratios of fuel-oxidizer velocity ($R$) of 1 and 5 (denoted R1 and R5, respectively; Fig. 2a and c) and the case of $N_2O$ at R = 3 (R3; Fig. 2d).

In the cases of $O_2$-enriched conditions, the R5 case exhibits a structure of dual flames, comprising an inner inverse diffusion flame and an outer normal diffusion flame, unlike the structure of a single flame in the R1 case. The maximum temperature in the R5 case exceeds that in the R1 case by over 450 K, reaching 2457 K, due to enhanced mixing of fuel and oxidizer near the rim of the central nozzle (Fig. 2c). A strong rate of heat release of 25 W is observed near the central nozzle in the R5 case, absent in the R1 case. Although the outer flame in the R5 case produces a weaker rate of heat release (5 W) compared to that in the R1 case (15 W), the increased velocity of the oxidizer inlet stretches the flame, extending the zone of high temperature to 14–17 mm in height above the burners (HABs), compared to 8–10 mm HABs in the R1 case (Fig. 2a and c). This elongation broadens the spatial distributions of $H_2O$ and $CO_2$, with maximum mole fractions of 0.219 and 0.094, respectively, in the R5 case. The distribution of $CO_2$ in the R5 case also extends to the region of the outer flame, aligning with the elevated temperatures in the zone of the inner flame.

For the case of $N_2O$ at R = 3, the decomposition of $N_2O$ generates a thermal effect that drives the formation of a structure of dual flames (Fig. 2d). The inner flame reaches a peak temperature of approximately 2778 K, significantly higher than the temperature of the outer flame and the maximum of 2457 K in the R1 case (Fig. 2b and d). A substantial rate of heat release of 45 W is sustained at the exit of the oxidizer tube in the inner flame, nine times higher than the 5 W of the outer flame (Fig. 2d). The zone of high temperature in the R3 case is more confined, spanning 0–6 mm longitudinally and 0–1.5 mm transversely, and is positioned further upstream compared to the R5 case (14–17 mm HABs). The intense inner flame in the R3 case reduces the overall height of the diffusion flame of the outer region, as shown in Fig. 3, compared to the broader region of high temperature in the R1 case (9–12 mm longitudinally, Fig. 2b).

The mole fractions of $CO_2$ and $H_2O$ in the outer flames of the R1 and R3 cases are similar, with maximum values of 0.094 and 0.219, respectively, but slightly lower in the R3 case due to the dominant consumption of $CH_4$ by the inner flame (Fig. 2b and d). In the R3 case, the structure of dual flames in the inner region intensifies the downstream distributions of $CO_2$ and $H_2O$, with regions of high $CO_2$ concentration located at the top of the outer flame along the centerline and regions of high $H_2O$ concentration near the inner flame, corresponding to the zone of high temperature (Fig. 2d). In contrast, the R5 case shows slightly higher concentrations of $CO_2$ and $H_2O$, reflecting the broader structure of the flame (Fig. 2c).

Comparing the structures of dual flames in the R5 case of $O_2$-enriched conditions and the R3 case of $N_2O$ (Fig. 2c and d), the $N_2O$ case achieves a higher temperature (2778 K vs. 2457 K) and greater rate of heat release (45 W vs. 25 W) despite a lower R value. This is attributed to the exothermic decomposition of $N_2O$, which concentrates heat release and temperature upstream, enhancing the intensity of combustion. The distributions of $CO_2$ and $H_2O$ remain comparable between the two cases, with zones of high concentration reflecting the respective structures of the flames.

### 3.2. Temperature, vector field, and species distribution near the nozzle rim

Figs. 4 and 5 provide a detailed analysis of the region surrounding the rim of the central nozzle, highlighting significant differences among the cases presented in Fig. 2. In Fig. 4, the left panel illustrates the distribution of temperature alongside vector fields of velocity, while the right panel shows the concentration profile of isocyanic acid (HNCO) combined with the distribution of hydroperoxyl ($HO_2$). The right panel also identifies the zone of preignition [48–50], which primarily influences oxidation at lower temperatures. Within this zone, hydroperoxides ($H_2O_2$) form at relatively low temperatures, ranging from 400 to 1000 K, through reaction R. 23 ($HO_2 + HO_2 \rightarrow H_2O_2 + O_2$) [23]. Consequently, $HO_2$ acts as a precursor for the identification of the preignition zone in flames of hydrocarbons. Additionally, the presence of HNCO provides evidence of the involvement of nitrous oxide ($N_2O$) in the combustion of hydrocarbons, likely resulting from reactions R. 540 REV ($HNCO + M \rightarrow NH + CO + M$) and R. 542 REV ($HNCO + O \rightarrow NCO + OH$). For example, in R. 540, NH originates from $N_2O$, while CO derives from the fuel.

The cases of oxygen-enriched ($O_2$-enriched, 67 % nitrogen ($N_2$) + 33 % oxygen ($O_2$)) conditions, specifically R1 and R5 (fuel-

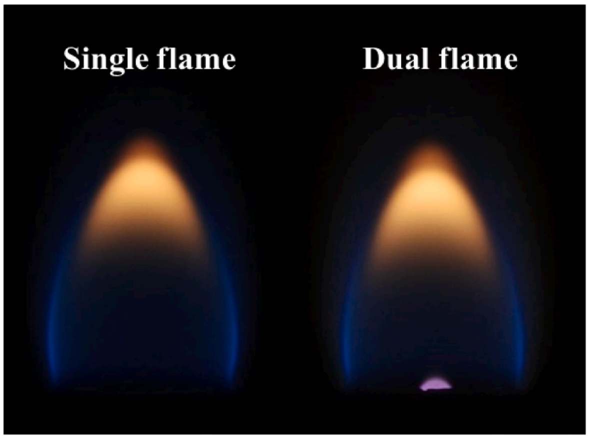

**Fig. 3.** Photographs illustrating the structures of single and dual flames in the diffusion of methane ($CH_4$) with nitrous oxide ($N_2O$).

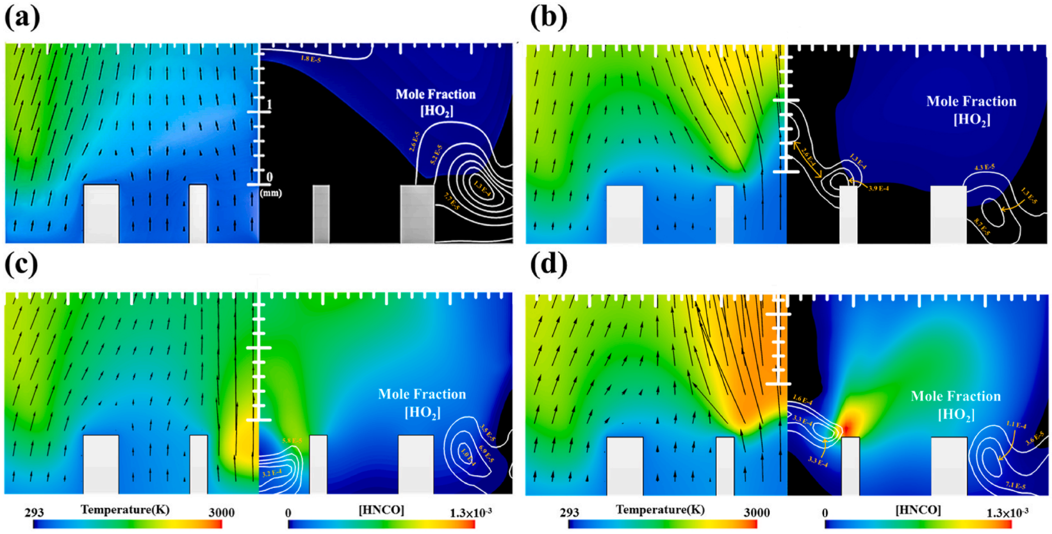

**Fig. 4.** The left panel illustrates the temperature with the velocity vector field, while the right panel shows the distribution of HNCO mole fraction combined with $HO_2$ mole fraction for the following cases: (a) an $O_2$-enriched mixture at R = 1, (b) an $O_2$-enriched mixture at R = 5, (c) $N_2O$ at R = 1, and (d) $N_2O$ at R = 3.

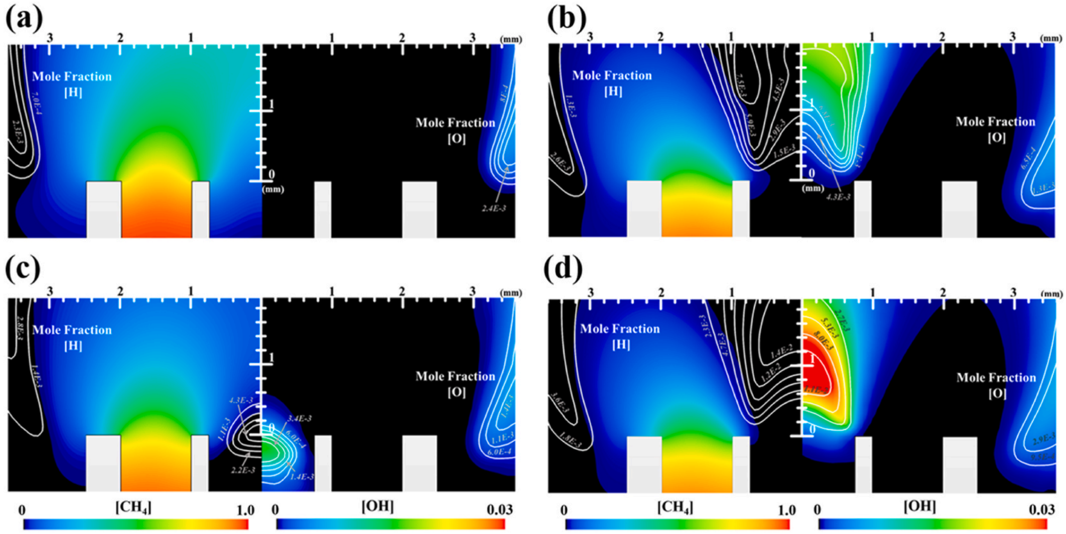

**Fig. 5.** Mole fraction of $CH_4$ overlaid with that of H (left) and mole fraction of OH overlaid with that of O (right) for (a) an $O_2$-enriched mixture when R = 1, (b) an $O_2$-enriched mixture when R = 5, (c) $N_2O$ when R = 1, and (d) $N_2O$ when R = 3.

oxidizer velocity ratio (R) of 1 and 5, respectively), exhibit notable differences. The left panels of Fig. 4a and b shows that the formation of an inner flame in the R5 case concentrates regions of high temperature near the exit of the central tube. This concentration induces thermal expansion, accelerating the fluid of the central region and intensifying the interaction between the oxidizer and the fuel compared to the R1 case. The distribution of velocity vectors in the left panel indicates a higher average magnitude in the R5 case than in the R1 case, suggesting more efficient mixing. The right panels reveal further distinctions. The concentrations of HNCO remain similar in both R1 and R5 cases, but the concentration of $HO_2$ differs markedly. In the R5 case, the concentration of $HO_2$ peaks at approximately $3.9 \times 10^{-4}$ near the rim of the central tube, a phenomenon absent in the R1 case (Fig. 4a) due to its structure of a single flame. This elevation in $HO_2$ concentration in the R5 case correlates with the location of the flame just downstream of the rim of the central nozzle.

Fig. 4c and d presents results for the $N_2O$ cases at R1 and R3, respectively. In the R1 case, the high temperature within the central tube, driven by the release of heat from the decomposition of $N_2O$, accelerates the velocity, drawing the fuel toward the centerline and facilitating mixing. In the R3 case, the formation of an inner flame significantly increases the velocity, further enhancing the mixing of fuel and oxidizer. The concentration of HNCO in the R3 case reaches a peak of $1.3 \times 10^{-3}$, higher than in the R1 case, but is largely

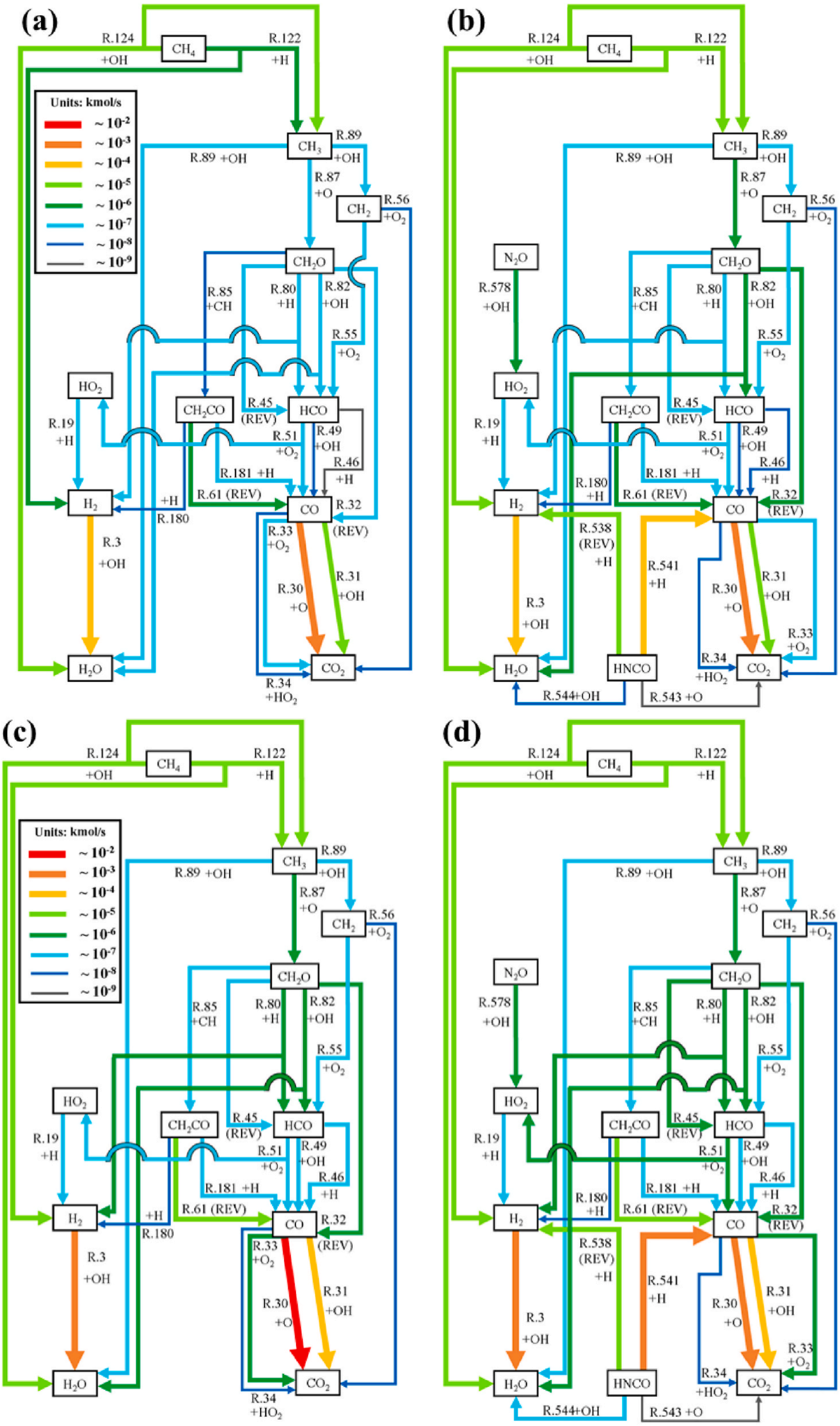

**Fig. 6.** Primary reaction pathways leading to the formation of $CO_2$ and $H_2O$ for (a) an $O_2$-enriched mixture at R = 1 [36], (b) $N_2O$ when R = 1, (c) an $O_2$-enriched mixture when R = 5 [36], and (d) $N_2O$ when R = 3.

depleted within the region of high temperature. In contrast, the R1 case shows a more uniform distribution of HNCO due to the absence of an inner flame. The inner flame in the R3 case positions $HO_2$ further downstream at the exit of the central nozzle (Fig. 4d). Notably, hydroxyl radicals (OH) react with $N_2O$ to form $HO_2$ via reaction R. 578 ($N_2O + OH \rightarrow N_2 + HO_2$). In the R3 case, the inner flame produces abundant OH radicals, which react with $N_2O$, leading to a significant accumulation of $HO_2$ near the exit of the central nozzle, with a maximum concentration of $5.0 \times 10^{-4}$ compared to $3.2 \times 10^{-4}$ in the R1 case. In the R1 case, the diffusion of methane ($CH_4$) results in dissociation into methyl ($CH_3$), formaldehyde ($CH_2O$), and formyl (HCO), while $N_2O$ dissociates into $O_2$, generating $HO_2$ within the central nozzle through reaction R. 51 ($HCO + O_2 \rightarrow CO + HO_2$).

A comparison of Fig. 4b and d, which depict the distributions of the mole fractions of HNCO and $HO_2$ in the $O_2$-enriched case (R = 5) and the $N_2O$ case (R = 3), elucidates the effects of the $N_2O$ oxidizer. The high temperature of the inner flame near the rim of the central nozzle in both cases increases the velocity of the fluid from the central tube (left panel). The $N_2O$ case exhibits a higher temperature and velocity than the $O_2$-enriched case, driven by the substantial release of heat from the decomposition of $N_2O$. This decomposition also triggers the formation of an inner flame in the $N_2O$ case at R = 1. The right panels of Fig. 4b and d shows similar distributions of $HO_2$ in both cases, but the $HO_2$ distribution extends further downstream in the $O_2$-enriched case due to the higher velocity of the oxidizer inlet. The maximum mole fraction of $HO_2$ in the outer region is $1.3 \times 10^{-4}$ in the $O_2$-enriched case and $1.1 \times 10^{-4}$ in the $N_2O$ case. In the inner region, the $O_2$-enriched case reaches a $HO_2$ concentration of $3.9 \times 10^{-4}$, three times that of the outer region, while the $N_2O$ case reaches $5.0 \times 10^{-4}$, nearly five times that of the outer region. Thus, the inner region of the $N_2O$ case exhibits a higher mole fraction of $HO_2$ than the $O_2$-enriched case, while the outer regions show comparable values. The concentration of HNCO, originating from reverse reactions R. 554 ($NH + NO \rightarrow N_2O + H$), R. 556 ($NH_2 + H \rightarrow NH + H_2$), and R. 558 ($NH_2 + OH \rightarrow NH + H_2O$), differs significantly between the two cases. In the $N_2O$ case, HNCO displays a broader distribution and higher concentration, with a maximum of approximately $1.3 \times 10^{-3}$, primarily in the zone of high temperature near the rim of the central nozzle, compared to the $O_2$-enriched case.

Fig. 5 illustrates the distributions of the mole fractions of $CH_4$ and associated radicals in the combustion of $CH_4$ with $N_2O$ and oxygen-enriched (67 % ($N_2$) + 33 % ($O_2$)) oxidizers. The left panel displays the mole fraction of $CH_4$ alongside that of H, while the right panel presents the mole fraction of O overlaid with that of OH. The results compare the $O_2$-enriched cases at fuel-oxidizer velocity ratios (R) of 1 and 5 (denoted R1 and R5, respectively; Fig. 5a and b) and the $N_2O$ cases at R = 1 and R = 3 (R1 and R3, respectively; Fig. 5c and d).

In the $O_2$-enriched cases, Fig. 5a and b highlight distinct behaviors between R1 and R5. In the zone of elevated temperature in the R5 case (left panel, Fig. 5b), the decomposition of $CH_4$ generates H radicals, reaching a peak mole fraction of approximately $7.5 \times 10^{-3}$ near the rim of the central nozzle. In contrast, the R1 case produces H radicals primarily in the outer region, with a lower concentration. A similar pattern emerges for OH and O radicals (right panel, Fig. 5b). In the R5 case, the dissociation of $O_2$ into O radicals, followed by their interaction with H radicals, produces OH radicals in the region of high temperature, with maximum mole fractions of 0.012 and $2.9 \times 10^{-3}$, respectively. The R1 case shows reduced radical formation in the inner region due to its structure of a single flame.

For the $N_2O$ cases, Fig. 5c and d reveal enhanced radical formation in the R3 case compared to the R1 case. In the R3 case (left panel, Fig. 5d), the decomposition of $CH_4$ within the zone of elevated temperature yields a significant concentration of H radicals, peaking at $1.4 \times 10^{-2}$ near the rim of the central nozzle. In contrast, the R1 case converts minimal $CH_4$ into H radicals, with a maximum mole fraction of $4.3 \times 10^{-3}$ inside the central tube (Fig. 5c). The right panels (Fig. 5c and d) show that the conversion of $N_2O$ into O radicals in the region of high temperature, with a maximum mole fraction of $1.1 \times 10^{-2}$, drives the production of OH radicals, reaching a peak of 0.03 in the R3 case. The R1 case exhibits lower intensities of these reactions, with reduced O and OH radical concentrations inside the central tube.

A comparison of Fig. 5b and d, representing the $O_2$-enriched case at R = 5 and the $N_2O$ case at R = 3, respectively, underscores the impact of the dual-flame structure observed in both cases (Fig. 2c and d). The decomposition of $CH_4$ in the zone of elevated temperature generates H radicals in the inner region of both cases, but the $N_2O$ case produces a greater accumulation, with a mole fraction of $1.4 \times 10^{-2}$ in the inner region compared to $7.5 \times 10^{-3}$ in the $O_2$-enriched case. In the outer region, the H radical mole fraction reaches $3.6 \times 10^{-3}$ in both cases. The peak H radical concentration occurs between 0.6 and 1 mm in the $O_2$-enriched case and between 0 and 0.6 mm in the $N_2O$ case, reflecting the upstream positioning of the inner flame in the $N_2O$ case.

The conditions of elevated temperature near the rim of the central nozzle promote the decomposition of the oxidizer, leading to the formation of OH and O radicals in the inner region of both cases. The distributions of these radicals follow similar patterns, but the $N_2O$ case exhibits higher mole fractions. In the $N_2O$ case, the maximum OH radical mole fraction reaches 0.012 in the outer region and 0.03 in the inner region, approximately 1.5 times higher than in the $O_2$-enriched case. Similarly, the O radical mole fraction peaks at $2.9 \times 10^{-3}$ in the outer region and $1.1 \times 10^{-2}$ in the inner region of the $N_2O$ case, nearly double the values in the $O_2$-enriched case. These differences highlight the enhanced radical production driven by the decomposition of $N_2O$ in the dual-flame structure.

### 3.3. Major reaction pathway

The concentrations and spatial distributions of $CO_2$ and $H_2O$ differed between the $O_2$-enriched and $N_2O$ cases, even with the same fuel flow rate. To explain these variations, the primary reaction pathways responsible for converting $CH_4$ into $CO_2$ and $H_2O$ were analyzed. Fig. 6 presents these key reaction pathways involved in product gas formation. The reaction constant ($k$) for each reaction is determined using the Arrhenius equation, given by:

$$k = AT^b \exp\left(-E_a/R_u T\right) \quad \text{Eq. 21}$$

The overall reaction rate follows a specific mathematical expression. Prior to this, the reaction rate ($\Delta\upsilon$) is derived from the molar concentration of the reactive species and the reaction constant. In this expression, $E_a$ denotes the activation energy, $b$ represents the temperature exponent, and $A$ corresponds to the pre-exponential factor.

$$\Delta\upsilon_{tot} = \iiint \Delta\upsilon(r,\theta,z)dV = \int_0^L \int_0^R 2\pi r \Delta\upsilon(r,z)drdz \qquad \text{Eq. 22}$$

Fig. 6 illustrates the primary reaction pathways for both the $N_2O$ and $O_2$-enriched cases; the reaction paths have similarities but different reaction rates. Initially, in both cases, $CH_4$ decomposed into $CH_3$, $H_2$, and $H_2O$ through R. 122 ($CH_4 + H \rightarrow CH_3 + H_2$) and R. 124 ($CH_4 + OH \rightarrow CH_3 + H_2O$). $H_2O$ was then produced by R. 3 ($H_2 + OH \rightarrow H_2O + H$). In the $CO_2$ formation pathway, $CH_3$ transforms into $CH_2O$ by R. 87 ($CH_3 + O \rightarrow CH_2O + H$) and is then converted into HCO by the R. 80 ($CH_2O + H \rightarrow H_2 + HCO$), R. 82 ($CH_2O + OH \rightarrow H_2O + HCO$), and reverse R. 45 ($H + HCO \rightarrow CH_2O$) reactions. CO is produced from HCO by R. 46 ($HCO + H \rightarrow H_2 + CO$), R. 49 ($HCO + OH \rightarrow H_2O + CO$), and R. 51. $CH_2CO$ is formed through R. 85 ($CH_2O + CH \rightarrow CH_2CO + H$), which contributes to the formation of CO through the R. 181 ($CH_2CO + H \rightarrow CO + CH_3$) and reversed R. 61 ($CO + CH_2 \rightarrow CH_2CO$) reactions. In the final stage, CO primarily converts into $CO_2$ through R. 30 ($CO + O \rightarrow CO_2$), R. 31 ($CO + OH \rightarrow CO_2 + H$), R. 33 ($CO + O_2 \rightarrow CO_2 + O$), and R. 34 ($CO + HO_2 \rightarrow CO_2 + OH$), especially R. 30 and R. 31. In the $O_2$-enriched condition, the R1 and R5 cases had structural variations, which led to substantial differences in the reaction intensities observed in these cases (Fig. 6a and c, resepectively). Reaction 122 (R. 122) was enhanced in the R5 case, which led to the production of additional $CH_3$ and $H_2$ from $CH_4$. This phenomenon caused Reactions 3 (R. 3) and 87 (R. 87) to intensify, which resulted in the production of additional $H_2O$ and $CH_2O$. As the formation of $CH_2O$ increased, additional HCO was formed through Reactions 80 (R. 80), 82 (R. 82), and the reverse of Reaction 45 (R. 45 REV). Consequently, additional CO was produced through Reactions 46 (R. 46) and 49 (R. 49) because of the enhanced HCO formation. The increased production of CO led to the formation of additional $CO_2$ through R. 30, R. 31, and R. 33. Moreover, the increased intensity of the R. 80 and R. 82 reactions resulted in the production of additional $H_2$ and $H_2O$ in the R5 case. The aforementioned results suggest that the existence of an inner flame in the R5 case (as shown in Fig. 2c) leads to more intense reactions and more heat release (up to 25 W) near the central nozzle rim.

Fig. 6b and d illustrate the reaction pathways for two R ratios with $N_2O$ as the oxidizer. The primary reaction pathways were the same for both R ratios; however, the reaction intensity increased because of the increased $N_2O$ input. This phenomenon caused an increase in the heat release in the reaction zone, which resulted in a more intense reaction. As depicted in Fig. 6d, Reactions 122 (R. 122) and 124 (R. 124) are responsible for the formation of $CH_3$ and $H_2$. $CH_3$ is subsequently converted into $CH_2O$ through Reactions 87 (R. 87) and 89 (R. 89). However, $CH_2O$ undergoes conversion into HCO through Reactions 80 (R. 80), 82 (R. 82), 85 (R. 85), and the reverse of Reaction 45 (R. 45 REV). In contrast to the R1 scenario, it is noteworthy that Reactions 80 (R. 80) and the reverse of Reaction 45 (R. 45 REV) become more pronounced in the R3 case, resulting in additional HCO production. Furthermore, Reactions 46 (R. 46), 49 (R. 49), and 51 (R. 51) are promoted due to the increased HCO production, leading to greater CO formation.

Moreover, an increase in the input of $N_2O$ facilitates the conversion of HNCO into CO through Reaction 541 (R. 541) and $H_2O$

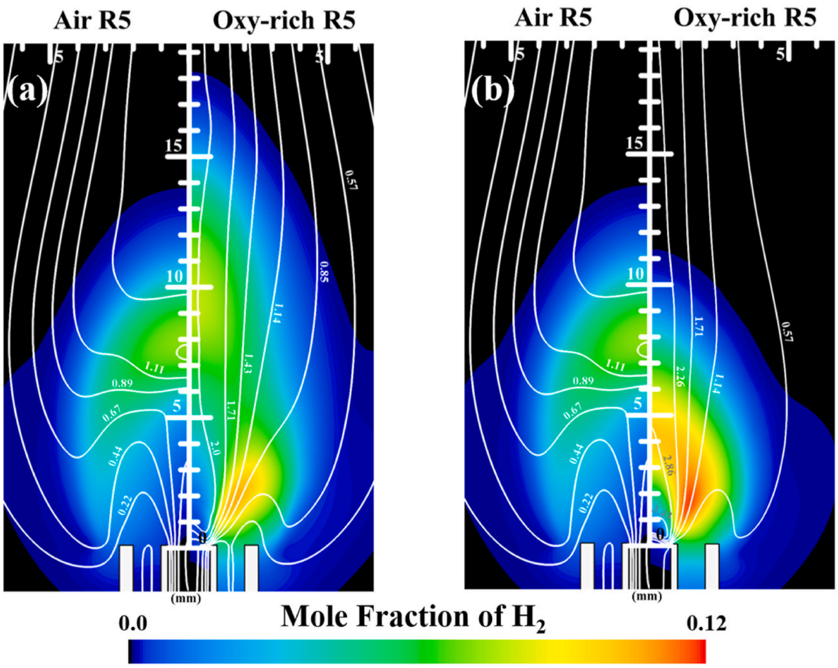

**Fig. 7.** Comparison of mole fractions of $H_2$: (a) between air and the oxygen-enriched case (67 % $N_2$ + 33 % $O_2$) at fuel-oxidizer velocity ratio (R) of 5, and (b) between air and the nitrous oxide ($N_2O$) case at R = 5 and R = 3.

through Reaction 544 (R. 544). The rise in CO concentration intensifies Reactions 31 (R. 31) and 33 (R. 33), resulting in an increased production of $CO_2$, as depicted in Fig. 6d. The enhancement of Reaction 80 (R. 80) leads to an increased generation of $H_2$, intensifying Reaction 3 (R. 3) and resulting in higher $H_2O$ generation when R equals 3.

Fig. 6c and d provide a comparison between the $O_2$-enriched and $N_2O$ cases, highlighting the different reaction pathways between the two conditions. Although the reactions in both cases had similar intensity because of the existence of a dual-flame structure in the cases, they exhibited some differences. The R. 45 REV and R. 51 reactions exhibited higher intensity in the $N_2O$ case compared to the $O_2$-enriched case, leading to an increased production of HCO, CO, and $HO_2$. However, despite CO formation being more significant in the $N_2O$ case compared to the $O_2$-enriched case, the intensity of the R. 30 reaction was relatively lower in the $N_2O$ case. Fig. 6d presents several reactions that dominated the major reaction pathway and produced more CO, $H_2$, $H_2O$, and $CO_2$ in the $N_2O$ case. These reactions included the reversed R. 538 ($H_2 + NCO \rightarrow HNCO + H$), R. 541 ($HNCO + H \rightarrow NH_2 + CO$), R. 543 ($HNCO + O \rightarrow NH + CO_2$), R. 544 ($HNCO + OH \rightarrow H_2O + NCO$), and R. 578 ($N_2O + OH \rightarrow N_2 + HO_2$) reactions. In general, the majority of reactions, particularly those involving $N_2O$, exhibited slightly greater intensity in the $N_2O$ case compared to the $O_2$-enriched case, despite the lower R ratio in the $N_2O$ case. Ultimately, the thermal impact of $N_2O$ decomposition enhances both the speed and intensity of the reaction at a specific R ratio.

Furthermore, the reaction pathways displayed in Fig. 6c and d indicate that $H_2$ production experiences an augmentation in the presence of $O_2$-enriched and $N_2O$ cases when the dual-flame structure is present. Specifically, Reactions 122 (R. 122) and 80 (R. 80)

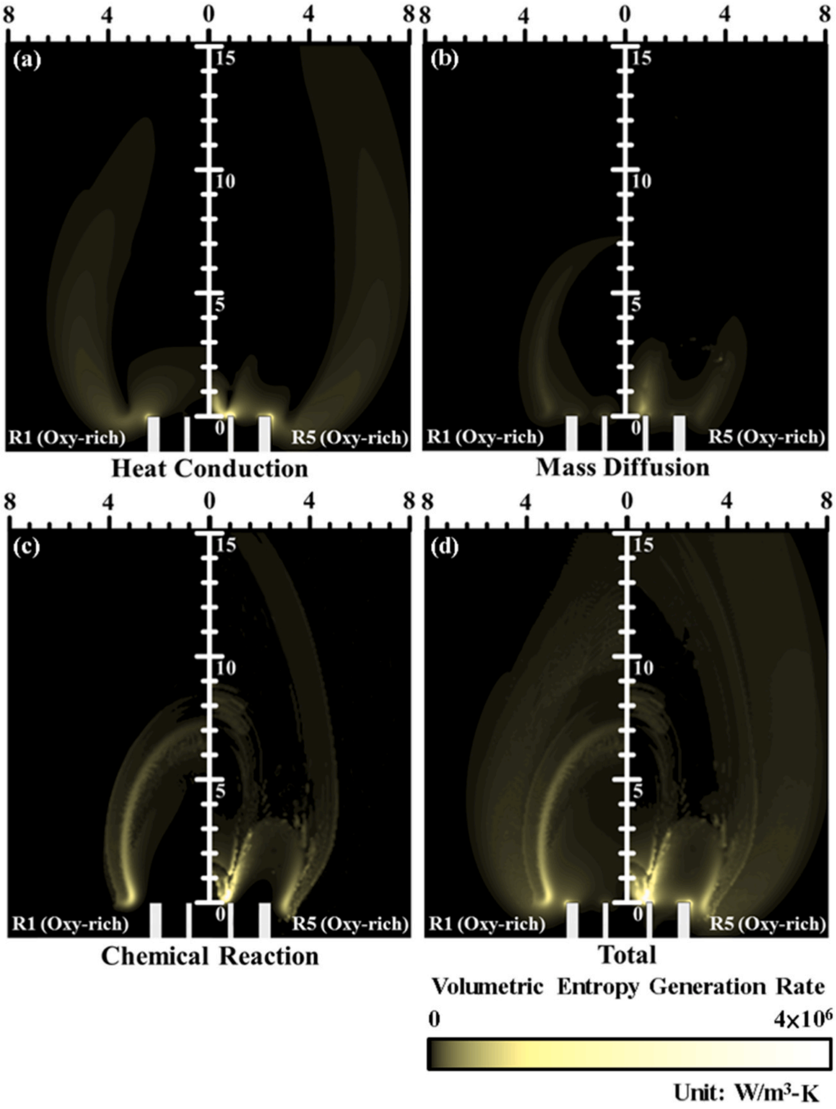

**Fig. 8.** Comparison of contributions to the rate of entropy generation (σ) in oxygen-enriched combustion (67 % $N_2$ + 33 % $O_2$) at fuel-oxidizer velocity ratios (R) of 1 (left) and 5 (right): (a) heat conduction, (b) mass diffusion, (c) chemical reactions, and (d) distribution of the total entropy generation rate.

exhibit greater intensity in the dual-flame instances (i.e., R = 3 and R = 5) compared to the single-flame instances (i.e., R = 1). The data presented in Fig. 7a and b support this finding, showing that the $H_2$ concentration reached higher levels in both the $O_2$-enriched case (peaking at approximately 0.09) and the $N_2O$ case (with a maximum of around 0.12) compared to the air-alone case, where the highest concentration was approximately 0.065. The increased $H_2$ concentration led to a higher burning velocity, which caused the inner flame to move upstream and reattach to the central nozzle rim. This resulted in the formation of the dual-flame structure observed in the $O_2$-enriched and $N_2O$ diffusion flames.

### 3.4. *Distribution of the entropy generation rate*

To investigate the effects of the decomposition of nitrous oxide ($N_2O$) and changes in flame structure on the rate of entropy generation ($\sigma$), numerical simulations are conducted using an oxygen-enriched mixture (67 % nitrogen ($N_2$) + 33 % oxygen ($O_2$)) and $N_2O$ as oxidizers. Figs. 8 and 9 illustrate the contributions of mass diffusion, chemical reactions, and heat conduction to the distribution of entropy generation rates, as well as the total entropy generation rate for different oxidizers and flame structures. The term associated with chemical reactions dominates within the main zone of reaction, while the term related to heat conduction exerts the greatest influence in regions of high temperature and near the nozzle, where steep gradients of temperature occur. The term linked to mass diffusion is primarily concentrated in the zone of reaction, characterized by intense chemical activity and significant variations in species concentrations.

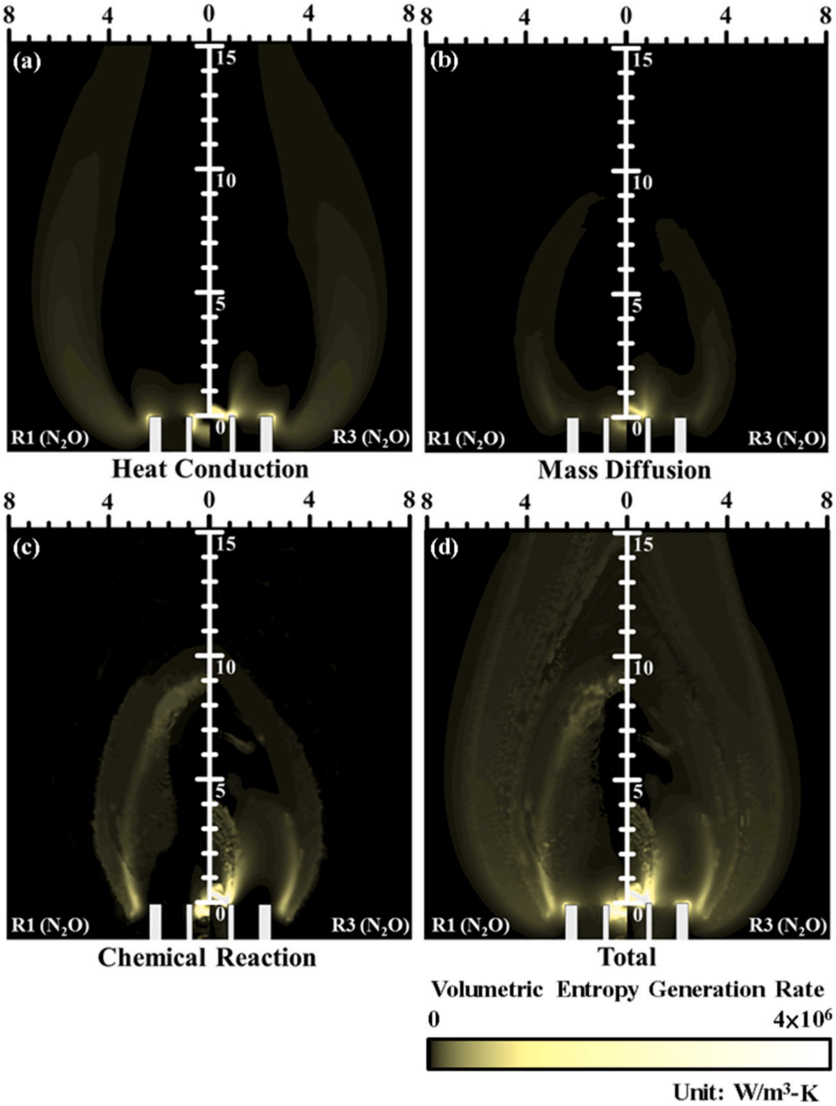

**Fig. 9.** Comparison of contributions to the rate of entropy generation (σ) in the $N_2O$ case at fuel-oxidizer velocity ratios (R) of 1 (left) and 3 (right): (a) heat conduction, (b) mass diffusion, (c) chemical reactions, and (d) distribution of the total entropy generation rate.

In the $O_2$-enriched case, an increase in the fuel-oxidizer velocity ratio (*R*) from 1 to 5 transforms the flame structure from a configuration of a single flame to a configuration of dual flames, as depicted in Fig. 2a and c. Fig. 8 illustrates the variation in the rates of entropy generation between these conditions, with Fig. 8d specifically highlighting significant differences in the distribution of entropy between the R1 and R5 cases. The highest entropy generation occurs near the rim of the central nozzle in the R5 case, whereas in the R1 case, it is observed closer to the rim of the fuel nozzle. The structure of dual flames in the R5 case intensifies chemical reactions, resulting in steeper gradients of species and elevated temperatures in the region surrounding the rim of the central nozzle. The combined contributions of heat conduction, mass diffusion, and chemical reactions increase the total entropy generation in the R5 case by a factor of 2.09 compared to the R1 case.

Under $O_2$-enriched conditions, the term associated with chemical reactions exerts the greatest influence in the R5 case, surpassing the term related to heat conduction by a factor of 1.13 and the term linked to mass diffusion by a factor of 3.81. The consumption of methane ($CH_4$) primarily by the inner flame in the R5 case weakens the chemical reactions in the outer flame compared to those in the R1 case. Consequently, the outer flame in the R1 case exhibits higher temperatures and steeper gradients of species than those in the R5 case. Fig. 8a, **b**, and **8c** demonstrate that in the R5 case, the highest entropy generation from chemical reactions, mass diffusion, and heat conduction concentrates near the rim of the fuel nozzle. The outer flame in the R5 case shows a slightly higher entropy generation than that in the R1 case. However, as the flow progresses downstream, the effects of chemical reactions, mass diffusion, and heat conduction diminish rapidly in the R5 case, falling below those observed in the R1 case. Within the structure of dual flames in the R5

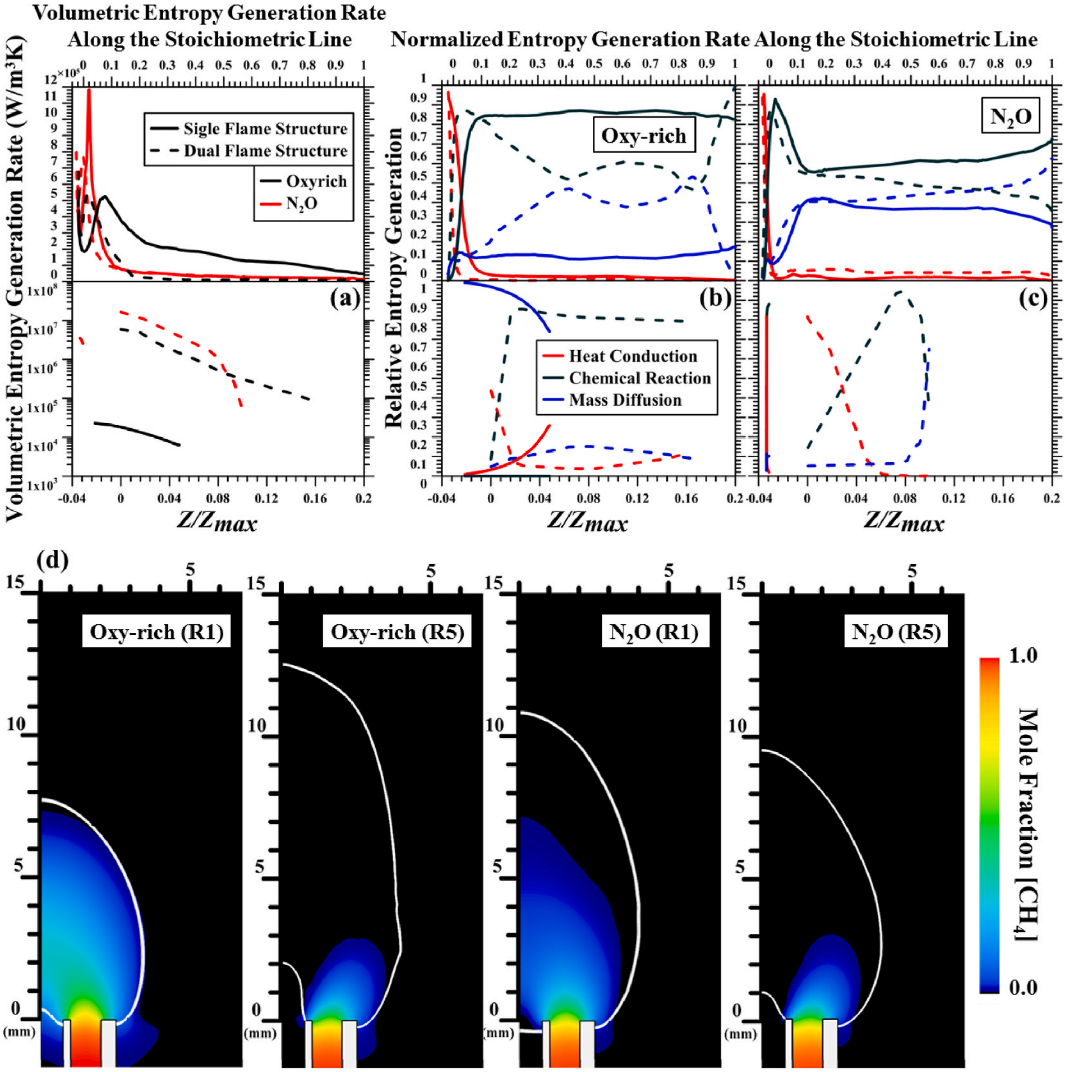

**Fig. 10.** Analysis of the rate of entropy generation (σ) along stoichiometric lines for oxygen-enriched (67 % $N_2$ + 33 % $O_2$) and $N_2O$ cases: (a) volumetric entropy generation rate along outer (top) and inner (bottom) stoichiometric lines at fuel-oxidizer velocity ratio (R) of 1, (b) contributions of heat conduction, mass diffusion, and chemical reactions in the $O_2$-enriched case at R = 1 and R = 5, (c) contributions in the $N_2O$ case at R = 1 and R = 3, and (d) illustration of inner and outer stoichiometric lines.

case, the term associated with chemical reactions remains the dominant contributor to entropy generation.

Fig. 9 compares the distributions of the rate of entropy generation ($\sigma$) for the nitrous oxide ($N_2O$) oxidizer at fuel-oxidizer velocity ratios (R) of 1 and 3 (R1 and R3, respectively), depicted in the left and right panels, respectively, revealing similar patterns in both cases. Fig. 9d indicates that the peak entropy generation occurs near the rim of the central nozzle in both cases, but in the R3 case, it is positioned further downstream, between 0 and 0.5 mm in height above the burners (*HABs*) along the axial direction. The formation of an inner flame in the R3 case intensifies chemical reactions, resulting in elevated temperatures and steeper gradients of species. Consequently, the contributions of heat conduction, mass diffusion, and chemical reactions to entropy generation increase in the R3 case, with the peak entropy generation reaching a value 4.78 times higher than that in the R1 case.

In both R1 and R3 cases, the term associated with chemical reactions dominates the entropy generation. However, the greater intensity of reactions in the R3 case enhances the relative contribution of this term compared to the R1 case. In the R3 case, the contribution of the chemical reaction term exceeds that of heat conduction by a factor of 2.70 and that of mass diffusion by a factor of 7.48. The region of high temperature generated by the inner flame in the R3 case transfers heat to the unburned gas, causing the outer flame to develop further upstream, consistent with the findings illustrated in Fig. 3. Fig. 9a, b, and **9c** show that the entropy generation from chemical reactions, mass diffusion, and heat conduction is confined to a more restricted area in the outer region of the R3 case compared to the R1 case.

The consumption of a portion of methane ($CH_4$) by the inner flame in the R3 case results in a slightly lower contribution of the chemical reaction term in the outer region compared to the R1 case, as depicted in Fig. 9c. In the outer region, the chemical reaction term reaches a peak value in the R1 case, 1.65 times greater than that in the R3 case. Despite this difference, the chemical reaction term remains the dominant contributor to entropy generation in both cases. The rate of entropy generation associated with chemical reactions is calculated for each major species, revealing variations in the final products of $CH_4$–$N_2O$ flames, particularly carbon dioxide ($CO_2$) and water ($H_2O$). Fig. 6d illustrates the primary reaction pathway from $CH_4$ to these final products in the R3 case, highlighting the enhancement of several reactions in this scenario.

Moreover, although both the $O_2$-enriched (R5) and $N_2O$ (R3) cases featured a dual-flame structure, the entropy generation was more significant in the $N_2O$ case. Specifically, the $N_2O$ case exhibited an overall entropy generation that was roughly 1.56 times higher, while the chemical reaction term was nearly double that of the $O_2$-enriched case. Although the intensity of the major reactions was similar between the two cases (Fig. 6c and d), several reactions in the $N_2O$ case contributed to a higher overall reaction intensity. This effect, combined with greater reaction intensity, led to steeper temperature and species gradients in the $N_2O$ case compared to the $O_2$-enriched case. As a result, the terms related to mass diffusion and heat conduction in the $N_2O$ case were approximately 1.30 and 1.11 times greater, respectively, than the corresponding values in the $O_2$-enriched case.

To evaluate the rate of entropy generation ($\sigma$) along the stoichiometric line, where the intensity of reactions is highest, the volumetric entropy generation rate is calculated following the methodology outlined in Ref. [51]. Fig. 10a presents the corresponding results. Fig. 10d illustrates two stoichiometric lines, one inside and one outside the fuel port, due to the presence of two oxidizers in the combustion of $CH_4$ with $N_2O$ and oxygen-enriched (67 % $N_2$ + 33 % $O_2$) oxidizers. In Fig. 10a, the top panel displays the outer stoichiometric line (coflow), while the bottom panel shows the inner stoichiometric line (oxidizer). To account for variations in flame heights between the $N_2O$ and $O_2$-enriched cases, the axial distance ($Z$) is normalized by expressing it as a fraction of the maximum axial distance ($Z/Z_{max}$).

Fig. 10a reveals that in the $N_2O$ case at a fuel-oxidizer velocity ratio (R) of 1, the highest entropy generation rate occurs at $Z/Z_{max} = 0.02$, reaching approximately $1.2 \times 10^6$ W/m$^3$·K. Beyond this peak, the rate declines sharply and stabilizes within the range of $5 \times 10^4$ to $7.5 \times 10^4$ W/m$^3$·K for $Z/Z_{max}$ values greater than 0.2. In contrast, the $O_2$-enriched case at R = 1 exhibits a peak entropy generation rate of about $5.3 \times 10^5$ W/m$^3$·K at $Z/Z_{max} = 0.072$, lower than that in the $N_2O$ case. This rate decreases gradually, reaching a minimum of approximately $5.0 \times 10^4$ W/m$^3$·K near the upper section of the stoichiometric line, distinct from the minimum values observed in the $N_2O$ case.

The peak entropy value for the $N_2O$ cases decreased when the R ratio increased, especially in the outer stoichiometric line (approximately $7.8 \times 10^5$ W/m$^3$ · K at $Z/Z_{max} = 0$ for the $N_2O$ case). However, for the $O_2$-enriched case, the peak value remained similar if the R ratio increased (about $5.5 \times 10^5$ W/m$^3$ · K at $Z/Z_{max} = 0.018$ for the $O_2$-enriched case) in the outer stoichiometric line. As depicted in Fig. 10a, the entropy generation rate in the $N_2O$ case at R = 1 reached a peak of approximately 2.6 × 106 W/m$^3$·K, with a more pronounced presence in regions upstream of the nozzle rim, as shown in the lower section. In contrast, for the $O_2$-enriched case at R = 1, the entropy generation rate declined as the flame height increased. The total entropy generation rate increased as the R ratio increased in the $O_2$-enriched and $N_2O$ cases. The peak values for the $O_2$-enriched and $N_2O$ cases were $6.0 \times 10^6$ and $1.9 \times 10^7$ W/m$^3$ · K, respectively. Although the trends for these two cases were similar, the entropy in the $N_2O$ case decreased faster than that in the other two cases as the axial location increased.

Fig. 10b and c illustrate how entropy generation varies along the outer and inner stoichiometric lines for different oxidizers and R ratios. In the upper section of Fig. 10b, total entropy generation is primarily influenced by the heat conduction term when $Z/Z_{max}$ <0 along the outer stoichiometric line. In contrast, when $Z/Z_{max}$ >0, the primary contributor to total entropy generation is the chemical reaction term. Additionally, in both the $O_2$-enriched and $N_2O$ cases at R = 1, the mass diffusion term has a greater impact on entropy generation compared to heat conduction.

In the $O_2$-enriched case at $R = 5$ (Fig. 10b), although variations occur in the contributions from chemical reactions and mass diffusion, the overall entropy generation along the outer stoichiometric line remains primarily influenced by chemical reactions. However, in the $N_2O$ case with R = 3 (Fig. 10c), the mass diffusion term becomes dominant when $Z/Z_{max} > 0.76$, and the chemical reaction term is no longer dominant along the outer stoichiometric line. In the lower sections of Fig. 10b and c, total entropy generation is primarily influenced by chemical reactions for both oxidizers due to the formation of an inner flame in these cases. In Fig. 10b, the mass diffusion term is the second most influential term between $Z/Z_{\max} = 0.02$ and 0.16. Outside this range, heat conduction emerges as the second most significant contributor in the $O_2$-enriched case. In contrast to the $O_2$-enriched case with R = 5 (Fig. 10b), in the $N_2O$ case with R = 3 (Fig. 10c), the chemical reaction term dominates between $Z/Z_{\max} = 0.02$ and 0.08. In regions below this range, heat conduction is the dominant contributor, whereas in regions above this range, mass diffusion becomes the primary influence along the inner stoichiometric line.

### 3.5. *Exergy*

The exergy, representing the useable energy in the combustion process, was examined for both the $O_2$-rich and $N_2O$ cases (Fig. 11) following the analysis of the volumetric entropy distribution. Fig. 11a displays the exergy consumed by irreversibility and the total exergy input in both cases. The total exergy values were 9073.6, 10286.7, 9225.4, and 10135.6 W for the $O_2$-enriched case with R = 1, the $O_2$-enriched case with R = 5, the $N_2O$ case with R = 1, and the $N_2O$ case with R = 3, respectively. Since $N_2O$ possesses greater chemical availability compared to the $O_2$-enriched mixture, the exergy input in the $N_2O$ case was correspondingly higher. The R1 and R5 $O_2$-enriched cases differed substantially. Although the total input energy was higher in the R5 case, the exergy in this case was almost equal to that in the R1 case, which indicated that the R5 case had lower efficiency. In the R5 case, the terms for chemical reaction, heat conduction, and mass diffusion were 2.5, 1.8, and 1.7 times higher, respectively, compared to those in the R1 case. The chemical reaction term was most different because of the more intense reaction in the R5 case, in which a dual-flame structure formed (as shown in Fig. 6a and c).

In the $N_2O$ case, the R ratio was adjusted from 1 to 3. Although the R3 case had greater energy than did the R1 case, the exergy in the R3 case was slightly lower because more exergy was consumed (approximately 1050 W more than in the R1 case). In the R3 case, the terms for chemical reaction, mass diffusion, and heat conduction were 1.6, 1.5, and 1.1 times higher, respectively, compared to those in the R1 case. The difference in the chemical reaction terms of the R1 and R3 cases accounted for approximately 81 % of the total exergy difference (approximately 850 W). This phenomenon was likely attributable to the greater heat release resulting from the greater $N_2O$ input, which increased the intensity of the overall reaction. Furthermore, the flame structure in the R3 case was a dual-flame structure, with two reaction regions being present in the flame, which led to a larger reaction zone and more intense reaction than those of the case of R1. Consequently, the chemical reaction term increased in the case of R3. Moreover, the chemical reaction term of the $N_2O$ case (R = 3) was almost twice that of the $O_2$-enriched case (R = 5) because of the more intense reaction attributed to $N_2O$, despite the similar energy input.

The exergy of the $O_2$-enriched and $N_2O$ combustion cases was analyzed. Fig. 11b illustrates the percentage contributions of chemical reaction, mass diffusion, and heat conduction terms to the incoming exergy. In the $O_2$-enriched case, the consumption of incoming exergy was primarily influenced by the chemical reaction term, which rose from 5.3 % at R = 1–11.6 % at R = 5 due to the intensified reaction induced by the dual-flame structure. In addition, the heat conduction term increased from 4.6 % when R = 1–7.4 % when R = 5 because of the higher temperature distribution in the R5 case (Fig. 2c). Consequently, the percentage of remaining energy, i.e., second law efficiency, decreased from 88.5 % when R = 1–78.8 % when R = 5 because of the increase in irreversibility in the R5 case. In the $N_2O$ case, the chemical reaction term had a high percentage contribution; however, the irreversibility produced by the chemical reaction in the R3 case (22.4 %) was considerably higher than that in the $O_2$-enriched R5 case (15.7 %) because of the more intense reaction of $N_2O$ (Fig. 6d) caused by the dual-flame structure. Moreover, the heat conduction term marginally increased from 7.8 % in the $O_2$-enriched R5 case to 8.3 % in the $N_2O$ R3 case. When the R ratio increased from 1 to 3 in the $N_2O$ case, the percentage of remaining energy, i.e. second law efficiency, decreased from 74.3 % to 66.3 %. The aforementioned results indicate that although the $N_2O$ case had higher total incoming exergy than did the $O_2$-enriched case, the irreversibility caused by the more intense reactions, particularly the chemical reaction term, resulted in lower remaining exergy and lower efficiency. Overall, the aforementioned findings indicate the importance of analyzing the exergy and the contribution of different terms to incoming energy when evaluating combustion processes.

## 4. Conclusions

This study underscores the importance of analyzing exergy and the contributions of various terms to incoming energy in the evaluation of combustion processes. Through comprehensive numerical simulations and detailed analysis of reaction mechanisms, the study investigates the effects of the decomposition of nitrous oxide ($N_2O$) and the fuel-oxidizer velocity ratio ($R$) on the thermal behavior of combustion processes. The key findings are summarized as follows:

An increase in the $R$ ratio to 5 in the oxygen-enriched (67 % $N_2$ + 33 % $O_2$) case induces the formation of a structure of dual flames, comprising an inner inverse diffusion flame and an outer normal diffusion flame. This structure establishes a zone of high temperature that enhances the mixing of fuel and oxidizer, resulting in reactions of greater intensity compared to those in air at the same R ratio.

The simulation results reveal that the decomposition of $N_2O$ generates a zone of high temperature near the rim of the central nozzle. Reactions associated with $N_2O$, particularly those involving the cyanato radical (NCO) and isocyanic acid (HNCO), exhibit slightly higher intensity in the $N_2O$ case compared to the $O_2$-enriched case, despite a lower R ratio of 3.

The study demonstrates that a higher rate of entropy generation ($\sigma$) leads to a reduction in exergy and a decrease in second-law efficiency ($\eta_{II}$) during combustion. Specifically, an increase in σ reduces $\eta_{II}$ from 88.5 % to 78.8 % in $O_2$-enriched cases and from 74.3 % to 66.3 % in $N_2O$ cases as the $R$ ratio rises. This reduction is more pronounced in structures of dual flames, where $\eta_{II}$ falls below 80 %, primarily due to contributions from heat conduction and chemical reactions.

The study relies exclusively on numerical simulations, without experimental work, to examine the structure of dual flames

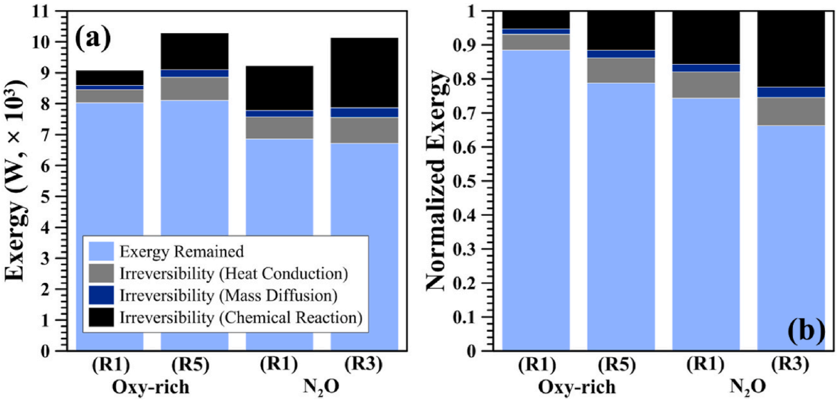

**Fig. 11.** Analysis of exergy in oxygen-enriched (67 % $N_2$ + 33 % $O_2$) and $N_2O$ cases: (a) total exergy input and consumption by irreversibility, and (b) percentage contributions of chemical reactions, mass diffusion, and heat conduction to incoming exergy.

generated by the diffusion of methane ($CH_4$) and $N_2O$. The strengths of this study lie in the thoroughness of its numerical simulations and the depth of its analysis of reaction mechanisms, which provide a comprehensive understanding of the combustion process of $CH_4$–$N_2O$ dual flames. These insights offer practical applications for optimizing combustion processes, enhancing efficiency, and minimizing energy loss. Furthermore, the study contributes to the theoretical foundation of combustion science, serving as a valuable reference for future research in this field.

The study concludes by emphasizing the importance of analyzing exergy and the contribution of different terms to incoming energy when evaluating combustion processes. The findings of the study are based on numerical simulations and detailed mechanism analysis to investigate the impact of $N_2O$ decomposition and R ratio on the combustion process's thermal behavior.

1. When the *R* ratio is increased to 5, introducing additional $O_2$ in the $O_2$-enriched case leads to the formation of a dual-flame structure. This results in a high-temperature zone that improves the fuel-oxidizer mixing and leads to more intense reactions than in air at the same R ratio.
2. The simulation results indicated that $N_2O$ decomposes and generates a high-temperature zone near the central nozzle rim. Reactions, particularly those associated with $N_2O$, including NCO- and HNCO-related reactions, exhibited slightly greater intensity in the $N_2O$ scenario than in the $O_2$-enriched condition, despite the lower R ratio.
3. The study also found that a higher entropy generation rate leads to a reduction in exergy during the combustion process and a decrease in second-law efficiency. The study revealed that increased entropy generation reduces exergy and decreases second-law efficiency from 88.5 % to 78.8 % in $O_2$-enriched cases and from 74.3 % to 66.3 % in $N_2O$ cases as the R ratio increases. This decrease is more pronounced in dual-flame structures, where efficiency drops below 80 %, primarily due to heat conduction and chemical reactions.

This study did not involve experimental work; instead, it conducted comprehensive numerical simulations on the structure of the dual flame generated by methane-nitrous oxide diffusion. The strengths of this study are rooted in its thorough numerical simulations and in-depth mechanism analysis, providing a deeper understanding of the $CH_4-N_2O$ dual-flame combustion process. These insights can be applied to improve combustion processes, resulting in increased efficiency and reduced energy loss. Furthermore, the study contributes to the theoretical foundation of combustion processes, serving as a valuable reference for future research in this field.

## CRediT authorship contribution statement

**Yueh-Heng Li:** Writing – review & editing, Supervision, Project administration, Methodology, Funding acquisition, Conceptualization. **Po-Hung Lin:** Writing – original draft, Software, Investigation, Formal analysis. **Wen-Yuan Tsai:** Writing – original draft, Software, Methodology, Investigation, Data curation. **Janusz Lasek:** Resources, Project administration, Investigation, Funding acquisition.

## Declaration of competing interest

All authors declared that: (i) no support, financial or otherwise, has been received from any organization that may have an interest in the submitted work; and (ii) there are no other relationships or activities that could appear to have influenced the submitted work.

## Acknowledgments

The authors gratefully acknowledge Professor Wen-Lih Chen for providing the numerical software. This study was financially supported by the National Science and Technology Council, Taiwan (NSTC 112-2923-E-006-002-MY3; NSTC 112-2221-E-006-106) and the National Centre for Research and Development, Poland (POLTAJ10/2022/49/MethaHydrAmmon/2023).

## Data availability

Data will be made available on request.

## References

[1] Y.-H. Li, J.-W. Liang, H.-J. Lin, Development of laminar burning velocity measurement system in premixed flames with hydrogen-content syngas or strong oxidizer conditions in a slot burner, Case Stud. Therm. Eng. 35 (2022) 102162, https://doi.org/10.1016/j.csite.2022.102162, 2022/07/01/.

[2] Y.-H. Li, J.-R. Hong, Power generation performance of hydrogen-fueled micro thermophotovoltaic reactor, Int. J. Hyd. Energy 43 (3) (2018) 1459–1469.

[3] Y.-H. Li, B.-C. Chuang, P.-H. Lin, J. Lasek, Effects of ammonia on combustion of coal in stoichiometric premixed methane–air flames, Fuel (Guildf.) 350 (2023/10/15/2023) 128825, https://doi.org/10.1016/j.fuel.2023.128825.

[4] Y. Sun, et al., RANS simulations on combustion and emission characteristics of a premixed NH3/H2 swirling flame with reduced chemical kinetic model, Chin. J. Aeronaut. 34 (12) (2021/12/01/2021) 17–27, https://doi.org/10.1016/j.cja.2020.11.017.

[5] C.-R. Yu, J.A. Cervera, C.-Y. Wu, Experimental study of the flame propagation of hydrogen-ammonia premixed fuels in porous media, J. Aeronautics, Astronautics and Aviation 55 (3) (2023) 335–345.

[6] W.-L. Chen, V. Sirisha, C.-Y. Yu, Y.-R. Wang, M.-W. Dai, J. Lasek, Design and optimization of a combined heat and power system with a fluidized-bed combustor and stirling engine, Energy 293 (2024) 130709.

[7] Y.-T. Wu, C.-W. Chang, P.-H. Lin, Y.-H. Li, J. Lasek, H.-K. Kan, Improving particle-burning efficiency of pulverized coal in new inclined jet burners, Int. J. Energy Res. 2024 (2024) 5372410.

[8] S. Fakudze, Y. Wei, Q. Shang, R. Ma, Y.-H. Li, J. Chen, P. Zhou, J. Han, C. Liu, Single-pot upgrading of run-of-mine coal and rice straw via Taguchi-optimized hydrothermal treatment: Fuel properties and synergistic effects, Energy 236 (2021) 121482.

[9] W.-L. Chen, C.-W. Huang, Y.-H. Li, C.-C. Kao, H.T. Cong, Biosyngas-fueled platinum reactor applied in micro combined heat and power system with a thermophotovoltaic array and stirling engine, Energy 194 (2020) 116862.

[10] Y.-H. Li, S. Pangestu, A. Purwanto, C.-T. Chen, Synergetic combustion behavior of aluminum and coal addition in hybrid iron-methane-air premixed flames, Combust. Flame 228 (2021) 364–374.

[11] Y.-H. Li, A. Purwanto, B.-C. Chuang, Micro-explosion mechanism of iron hybrid methane-air premixed flames, Fuel 325 (2022) 1124841.

[12] G.-B. Chen, Y.-H. Li, T.-S. Cheng, Y.-C. Chao, Chemical effect of hydrogen peroxide addition on characteristics of methane-air combustion, Energy 55 (2013) 564–570.

[13] Zakwan Azizi, Ahmad Hussein, Abdul Hamid, Jamaliah MD Said, Investigating the effects of metal additives on the mechanical properties of ammonium perchlorate/sorbitol solid rocket propellants, J. Aeronautics, Astronautics and Aviation 57 (3) (2024) 363–368.

[14] A.E. Nosseir, A. Cervone, A. Pasini, Review of state-of-the-art green monopropellants: for propulsion systems analysts and designers, Aerospace 8 (1) (2021) 20.

[15] Y.-H. Li, C. Chun-Han, M. Ilbas, Effect of diluent addition on combustion characteristics of methane/nitrous oxide inverse tri-coflow diffusion flames, Combust. Sci. Technol. 194 (10) (2022/07/27 2022) 1973–1993, https://doi.org/10.1080/00102202.2020.1854236.

[16] B.N. Villanueva, P.-H. Lin, Y.-H. Li, J.P. Honra, Effect of plasma assisted combustion on emissions of a premixed nitrous oxide fuel blend, Result. Eng. 25 (2025) 104251.

[17] M. Kawalec, P. Wolański, W. Perkowski, A. Bilar, Development of a liquid-propellant rocket powered by a rotating detonation engine, J. Propul. Power (2023) 1–8.

[18] S. Carlotti, F. Maggi, Evaluating new liquid storable bipropellants: safety and performance assessments, Aerospace 9 (10) (2022) 561.

[19] J. Vandooren, M. Branch, P. Van Tiggelen, Comparisons of the structure of stoichiometric CH4• N2O• Ar and CH4• O2• Ar flames by molecular beam sampling and mass spectrometric analysis, Combust. Flame 90 (3–4) (1992) 247–258.

[20] T. Newman-Lehman, R. Grana, K. Seshadri, F. Williams, The structure and extinction of nonpremixed methane/nitrous oxide and ethane/nitrous oxide flames, Proc. Combust. Inst. 34 (2) (2013) 2147–2153.

[21] O. Powell, P. Papas, C. Dreyer, Laminar burning velocities for hydrogen-, methane-, acetylene-, and propane-nitrous oxide flames, Combust. Sci. Technol. 181 (7) (2009) 917–936.

[22] D. Razus, M. Mitu, V. Giurcan, C. Movileanu, D. Oancea, Methane-unconventional oxidant flames. Laminar burning velocities of nitrogen-diluted methane–N2O mixtures, Process Saf. Environ. Prot. 114 (2018) 240–250.

[23] Z. Wang, O. Herbinet, N. Hansen, F. Battin-Leclerc, Exploring hydroperoxides in combustion: history, recent advances and perspectives, Prog. Energy Combust. Sci. 73 (2019) 132–181.

[24] A.Y. Shebeko, Y.N. Shebeko, A.V. Zuban', V.Y. Navtsenya, V.V. Azatyan, Influence on fluorocarbons flammability limits in the mixtures of H2-N2O and CH4-N2O, Russ. J. Phys. Chem. B 8 (1) (2014/01/01 2014) 65–70, https://doi.org/10.1134/S1990793114010072.

[25] Y.-H. Li, S.K. Reddy, C.-H. Chen, Effects of the nitrous oxide decomposition reaction on soot precursors in nitrous oxide/ethylene diffusion flames, Energy (Calg.) 235 (2021/11/15/2021) 121364, https://doi.org/10.1016/j.energy.2021.121364.

[26] Y.-H. Li, C.-H. Hsu, P.-H. Lin, C.-H. Chen, Thermal effect and oxygen-enriched effect of N2O decomposition on soot formation in ethylene diffusion flames, Fuel (Guildf.) 329 (2022) 125430.

[27] C.-H. Chen, Y.-H. Li, Role of N2O and equivalence ratio on NOx formation of methane/nitrous oxide premixed flames, Combust. Flame 223 (2021) 42–54.

[28] T. Cai, D. Zhao, N. Karimi, Optimizing thermal performance and exergy efficiency in hydrogen-fueled meso-combustors by applying a bluff-body, J. Clean. Prod. 311 (2021) 127573.

[29] Y. Guan, S. Becker, D. Zhao, J. Xu, M. Shahsavari, J. Schluter, Entropy generation and CO2 emission in presence of pulsating oscillations in a bifurcating thermoacoustic combustor with a Helmholtz resonator at off-design conditions, Aero. Sci. Technol. 136 (2023) 108204.

[30] V.S. Arpaci, A. Selamet, Entropy production in flames, Combust. Flame 73 (3) (1988) 251–259.

[31] K. Nishida, T. Takagi, S. Kinoshita, Analysis of entropy generation and exergy loss during combustion, Proc. Combust. Inst. 29 (1) (2002/01/01/2002) 869–874, https://doi.org/10.1016/S1540-7489(02)80111-0.

[32] M. Safari, F. Hadi, M.R.H. Sheikhi, Progress in the prediction of entropy generation in turbulent reacting flows using large eddy simulation, Entropy 16 (10) (2014) 5159–5177.

[33] M. Mehdi Safari, R.H. Sheikhi, M. Janbozorgi, H. Metghalchi, Entropy transport equation in large eddy simulation for exergy analysis of turbulent combustion systems, Entropy 12 (3) (2010) 434–444.

[34] K. Yamamoto, Y. Isobe, N. Hayashi, H. Yamashita, S.H. Chung, Behaviors of tribrachial edge flames and their interactions in a triple-port burner, Combust. Flame 162 (5) (2015) 1653–1659.

[35] K. Yamamoto, S. Kato, Y. Isobe, N. Hayashi, H. Yamashita, Lifted flame structure of coannular jet flames in a triple port burner, Proc. Combust. Inst. 33 (1) (2011) 1195–1201.

[36] D. Chou, W.-Y. Tsai, M.D. Emami, Y.-H. Li, Entropy generation and exergy assessment of methane–nitrous oxide diffusion flames in a triple-port burner, Int. J. Energy Res. 2023 (2023) 5364917.

[37] C.-R. Yu, C.-Y. Wu, An empirical formula to predict the overall irreversibility of counter-flow premixed flames of methane and its mixtures, Journal of Thermal Analysis and Calorimetry 147 (24) (2022) 14587–14599.

[38] A. Datta, Effects of gravity on structure and entropy generation of confined laminar diffusion flames, Int. J. Therm. Sci. 44 (5) (2005) 429–440.
[39] Z. Zhang, C. Lou, Y. Long, B.M. Kumfer, Thermodynamics second-law analysis of hydrocarbon diffusion flames: effects of soot and temperature, Combust. Flame 234 (2021) 111618.
[40] Y. Wenming, J. Dongyue, C.K.Y. Kenny, Z. Dan, P. Jianfeng, Combustion process and entropy generation in a novel microcombustor with a block insert, Chemical Engineering Journal 274 (2015) 231–237.
[41] D. Liu, H. Wang, Y. Zhang, H. Liu, Z. Zheng, M. Yao, On the entropy generation and exergy loss of laminar premixed flame under engine-relevant conditions, Fuel (Guildf.) 283 (2021) 119245.
[42] B.E. Poling, J.M. Prausnitz, J.P. O'connell, The Properties of Gases and Liquids, Mcgraw-hill, New York, 2001.
[43] W. Wang, H. Zhang, Laminar burning velocities of C2H4/N2O flames: experimental study and its chemical kinetics mechanism, Combust. Flame 202 (2019) 362–375.
[44] H. Wang, A. Laskin, A Comprehensive Kinetic Model of Ethylene and Acetylene Oxidation at High Temperatures, Progress report for an AFOSR new world vista program, 1998.
[45] C.R. Group, The San Diego mechanism: chemical kinetic mechanisms for combustion applications, in: Mechanical and Aerospace Engineering (Combustion Research), University of California, at San Diego, CA, 2014. http://web.eng.ucsd.edu/mae/groups/combustion/mechanism.html.
[46] A. Bejan, Advanced Engineering Thermodynamics, John Wiley & Sons, 2016.
[47] M.J. Moran, H.N. Shapiro, D.D. Boettner, M.B. Bailey, Fundamentals of Engineering Thermodynamics, John Wiley & Sons, 2010.
[48] S.M. Al-Noman, S.K. Choi, S.H. Chung, Numerical study of laminar nonpremixed methane flames in coflow jets: autoignited lifted flames with tribrachial edges and MILD combustion at elevated temperatures, Combust. Flame 171 (2016) 119–132.
[49] M. Frenklach, D.E. Bornside, Shock-initiated ignition in methane-propane mixtures, Combust. Flame 56 (1) (1984) 1–27.
[50] M. Altarawneh, B.Z. Dlugogorski, E.M. Kennedy, J.C. Mackie, Theoretical study of reactions of HO2 in low-temperature oxidation of benzene, Combust. Flame 157 (7) (2010) 1325–1330.
[51] A.M. Briones, S.K. Aggarwal, V.R. Katta, Effects of H2 enrichment on the propagation characteristics of CH4–air triple flames, Combust. Flame 153 (3) (2008) 367–383.